Topography optimisation using a reduced-dimensional model for transient conjugate heat transfer between fluid channels and solid plates with volumetric heat source

Yupeng Sun, Song Yao, Joe Alexandersen

Topography optimisation using a reduced-dimensional model for transient conjugate heat transfer between fluid channels and solid plates with volumetric heat source

Yupeng Sun[1,1], Song Yao[1], Joe Alexandersen[1*]

[1]Key Laboratory of Traffic Safety on Track of Ministry of Education, Central South University, Changsha, 410000, Hunan, China.
[2*]Department of Mechanical and Electrical Engineering, University of Southern Denmark, Odense, DK-5230, Denmark.

*Corresponding author(s). E-mail(s): joal@sdu.dk;
Contributing authors: yupeng_sun@csu.edu.cn; song_yao@csu.edu.cn;

Abstract

Consideration of transient effects is important for industrial applications of heat transfer structure optimisation studies, however, the huge computational cost associated with transient problems is a pressing concern. This paper proposes an extension of a previous reduced-dimensional model to transient conjugate heat transfer between a fluid flow and solid heated plates in a plate heat exchanger. The extended reduced-dimensional model introduces the temperature field of the plate governed by the heat conduction equation, which is coupled to the temperature field of the fluid, governed by the convection-diffusion equation, through the heat flux balance equation at the contact surface. The model is based on assumptions of fully-developed flow and constant temperature profile, reducing the three-dimensional problem to a planar problem and significantly reducing computational costs. The accuracy of the model for transient heat transfer simulation is verified by comparison with a three-dimensional model. In this paper, the topography of the heat exchanger plate is optimised for both steady-state and transient conditions by applying the reduced-dimensional model, resulting in topography-optimised designs with significantly improved performance compared to the reference design. The effectiveness of the optimised design was demonstrated by the cross-check of both the reduced-dimensional and full three-dimensional models. Compared to steady optimised design, transient optimised design demonstrates the impact of transient effects on optimisation results and the implications of considering transients are discussed.

Keywords: Topography optimisation, topology optimisation, transient optimisation, conjugate heat transfer, reduced-order model

1 Introduction

Plate heat exchangers are widely used in energy systems in the automotive, industrial, and construction sectors due to their compact structure and high heat transfer efficiency. A plate heat exchanger consists of a set of parallel plates with undulating surfaces. The plates form multi-layered channels between them, and heat is rapidly exchanged between the stationary medium inside

the plates and the fluid medium in the channels. The topography of the plate surface significantly affects the heat transfer efficiency, and optimising the topography of the plates can significantly increase the heat transfer area and thus the overall heat transfer efficiency.

Structural optimisation for plate heat exchangers has attracted a great deal of attention over the decades (Abou Elmaaty et al, 2017), and a lot of numerical techniques have been used for structural optimisation of plate heat exchangers, such as size optimisation and shape optimisation. Zhu et al (2023) used non-dominated sorting genetic algorithm to optimise the structural parameters of a plate-fin heat exchanger and then verified the optimised design with simulations and experiments. Tong et al (2022) used a combination of genetic and particle swarm algorithms to optimise the dimensions of a pillow plate heat exchanger. Although all of the studies described above improved the performance of the heat exchanger compared to the original design, none of them were independent of the initial design, and the optimisation results were based heavily on the a priori design.

Topology optimisation has a larger design space than size and shape optimisation, allowing for non-intuitive designs that are independent of the initial design, offering better designs at the initial design stage. Consequently, topology optimisation has received continuous attention and rapid development. In the field of conjugate heat transfer, significant progress has been made in topology optimisation research (Dbouk, 2017; Alexandersen and Andreasen, 2020; Fawaz et al, 2022), including studies on forced convection (Yoon, 2010) and natural convection (Alexandersen et al, 2014). Currently, most of the existing work focuses on steady-state heat transfer problems, with few studies investigating transient heat transfer optimisation problems. In many practical engineering heat transfer scenarios, boundary conditions often vary with time or have time-varying temperature responses as evaluation criteria. This requires considering transient effects on heat transfer optimisation, which is a future direction for industrial applications. Some research has already been conducted on transient heat transfer optimisation for thermal-fluid problems. For instance, Coffin and Maute (2016) proposed a topology optimisation method based on an explicit level set method for two- and three-dimensional steady-state and transient natural convection problems. Pizzolato et al (2017) utilised topology optimisation and multiphase computational fluid dynamics to develop efficient high-conductivity fin shapes to enhance the heat transfer of shell-and-tube latent heat energy storage devices. Pizzolato et al (2020) optimised the fin shapes of a multi-tube latent heat storage device and demonstrated its manufacturability through additive manufacturing. Yaji et al (2018) proposed a topology optimisation method based on the level set method and the lattice Boltzmann method, combined with the local-in-time adjoint-based method and parallel computing, to study the topology optimisation of large-scale unsteady thermal fluids. Their approach was recently extended to solve unsteady natural convection problem (Tanabe et al, 2023). Lundgaard et al (2019) proposed a design method based on density-based topology optimisation and a transient potential flow model coupled with heat transfer to optimise the distribution of two materials with different thermal properties in a two-dimensional design space to improve the performance of thermal energy storage systems.

All of the above-mentioned studies have pointed out the computational challenges associated with transient heat transfer optimisation (Alexandersen and Andreasen, 2020; Dbouk, 2017), especially for complex heat transfer phenomena. Considering transient effects significantly increases the computational cost, and topology optimisation requires hundreds or thousands of iterations, which further makes the computational cost a bottleneck for transient problems, Therefore, proposing and using simplified models to reduce the computational cost of transient heat transfer for optimisation becomes a viable solution.

In recent years, there has been increasing interest and development in the study of reduced-dimensional models for optimisation of conjugate heat transfer. These models simplify three-dimensional heat transfer problems into two-dimensional problems involving planar thermal fluids and solids based on reasonable assumptions and simplifications. Haertel et al (2018) proposed a pseudo-3D model for designing an air-cooled forced convection heatsink. Zeng et al (2018) used the pseudo-3D model to optimise the topology of

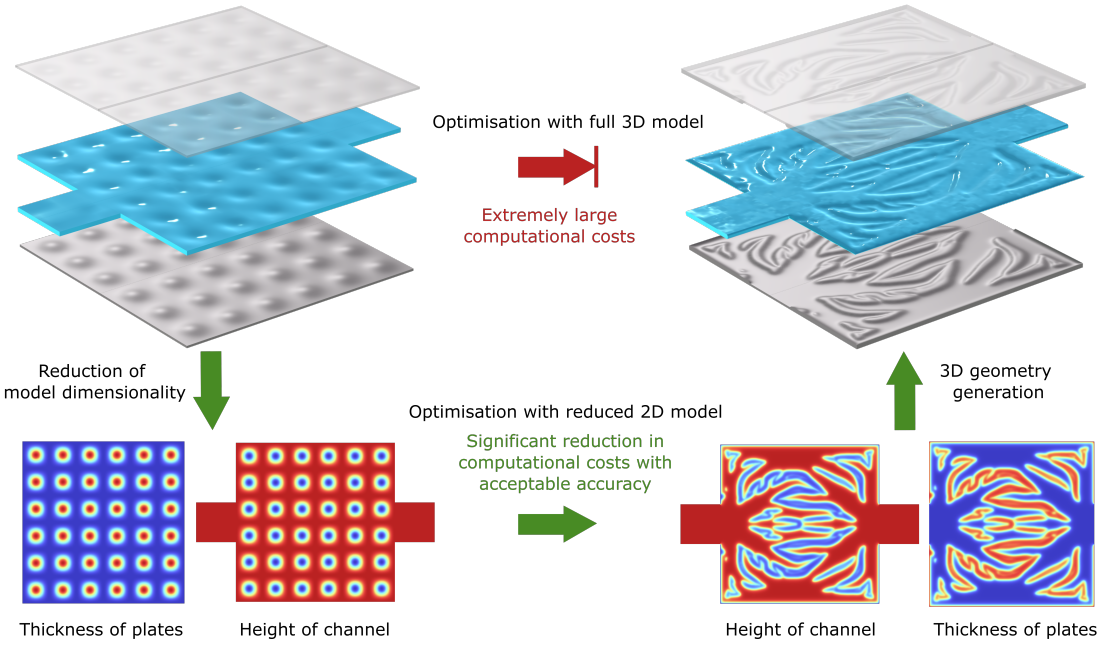

Fig. 1: Graphical overview of the application of reduced-dimensional model for structural topography optimisation.

air-cooled heat sinks and liquid-cooled microfluidic heat sinks (Zeng and Lee, 2019) and validate their performance through fabrication and experiments. Yan et al (2019) proposed a two-layer model based on the assumption of planar flow including the out-of-plane resistance and including the temperature in the base plate. Zeng et al (2020) proposed a transient pseudo-3D model to optimise the chip heat sink and validate the performance of the transient design. Zhao et al (2021a) proposed a multi-layer model based on similar ideas using a varying temperature profile function, applied it to the design of fin plate heat sinks, and considered turbulence effects in a subsequent study (Zhao et al, 2021b). In these studies, the optimised structure was an extruded structure with the same height, which was suitable for fin-type heat sinks but not for plate-type heat exchangers. Sun et al (2022) proposed a novel reduced-dimensional model that enables the optimisation of varying-height designs for plate-type heat exchangers. This model offers low computational cost and can generate optimised designs with continuously-varying heights, although it only considers the temperature field of the internal fluid while assuming a constant temperature of the solid plate. Although the studies mentioned above have attempted to reduce the computational cost of topology optimisation for heat transfer, only the work proposed by Zeng et al (2020) applied reduced models to transient optimisation for heat transfer. Thus, there is an urgent need for further research on reduced-dimensional models that consider transient effects to better reflect the significance of these modelling studies and aid in optimising real industrial problems.

This paper presents an extended reduced-dimensional model for transient forced convection between fluid flow and solid heated plates in plate heat exchangers, based on the model previously proposed by Alexandersen (2022) and Sun et al (2022). The inspiration for the previous and current work is the design of a thermal energy storage module (Veje et al, 2019; Dallaire et al, 2022; Hassan et al, 2023). The present work, with the goal of maximising the energy extracted from volumetrically heated plates, is a first step towards extracting latent energy stored in a phase change material.

The extended reduced-dimensional model introduces the temperature field of the plates governed by the heat conduction equation, coupled

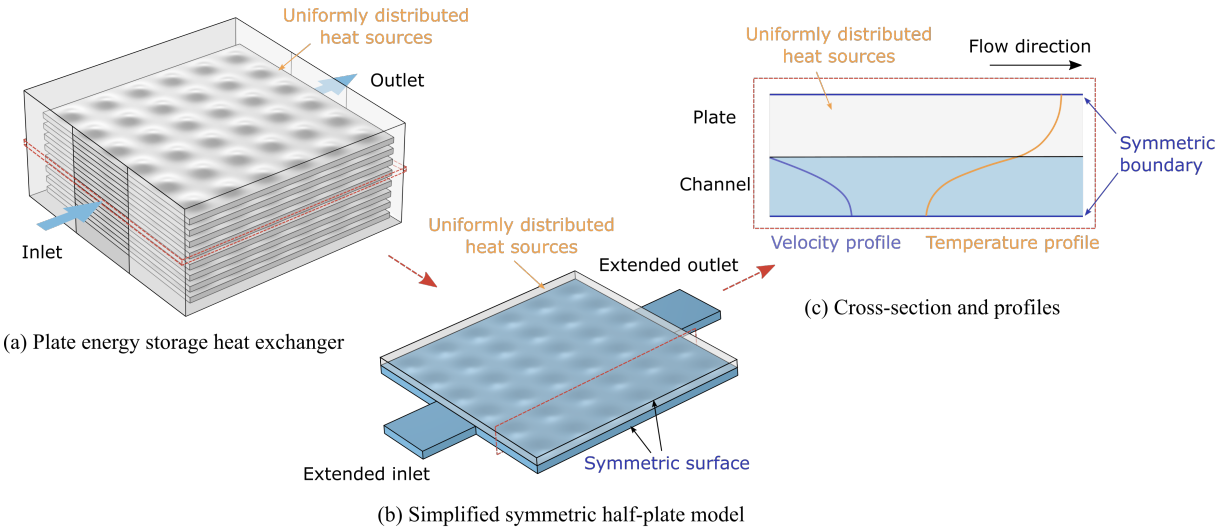

Fig. 2: Schematic diagram of the plate storage heat exchanger and the heat exchanger plate model.

with the temperature field of the fluid governed by the convection-diffusion equation, through the heat flux balance equation at the exchange surface. Furthermore, the extended model considers transient effects and can accurately simulate the transient temperature distribution of the system. This paper performs steady-state and transient optimisation of the topography of a three-dimensional heat exchanger plate with the objective of minimising the mean temperature of the plate. The designs obtained using the reduced-dimensional model are verified by using a three-dimensional model, and the significance of transient optimisation for practical industrial problems is investigated by comparing steady-state and transient optimisation. Fig. 1 provides a graphical overview of the proposed method for optimising the structural topography using the reduced-dimensional model. As will be demonstrated through this paper, the optimised designs obtained using this method exhibit significantly better performance under both steady-state and transient conditions than a reference design.

The rest of the paper is organised as follows: Section 2 derives and presents a reduced-dimensional model for the transient forced convection problem; Section 3 takes the plate heat exchanger in thermal energy storage systems as an example and verifies the accuracy of the reduced-dimensional model by comparing it with a full three-dimensional model; Section 4 gives implementation details of topology optimisation combined with the reduced-dimensional model, and the optimisation problem is formulated; Section 5 shows the optimised designs obtained for steady-state and transient heat transfer and compares them; Section 6 draws conclusions and presents future research work.

2 Reduced-dimensional model

Figure 2 shows a schematic diagram of a plate energy storage heat exchanger, which consists of a stack of plates with undulating surfaces, with fluid flowing between the plates at a certain velocity and exchanging heat with the plate surface by forced convection. The energy storage plates are simplified as solid plates with an internal heat source that exchanges heat with the surfaces by heat conduction, replacing stored energy with the simpler generated energy as an initial approximation. Due to its symmetry, the present work investigates the structure shown in Fig. 2, which consists of the half of the fluid channel and the half of the plate in contact with it, with symmetric boundaries on both the top and bottom surfaces.

Since the planar dimensions of the solid plate and fluid channel are significantly larger than their heights, the flow in the channel can be reduced

to a Poiseuille flow, with the velocity and temperature profiles of the fluid and the temperature profile of the solid assumed to remain constant in the flow direction as shown in Fig. 2. Furthermore, the following assumptions are made during the derivation of the reduced-dimensional model: (1) the flow in the channel is incompressible, fully-developed laminar flow; (2) the material properties of the fluid and solid are independent of the temperature; (3) inaccuracies in the temperature and velocity profiles introduced by height variations are negligible, ensured by constraining the height gradient during optimisation as discussed later.

2.1 Reduced-dimensional models for fluid flow

This paper extends the reduced-dimensional model for steady-state flow (Alexandersen, 2022) and makes uses of a reduced-dimensional model for transient flow first presented by Sun et al (2023):

$$\widetilde{\rho}_\mathrm{f}\frac{\partial \bar{u}_i}{\partial t} + \bar{\rho}_\mathrm{f}\bar{u}_j\frac{\partial \bar{u}_i}{\partial x_j} - \mu\frac{\partial}{\partial x_j}\left(\frac{\partial \bar{u}_i}{\partial x_j} + \frac{\partial \bar{u}_j}{\partial x_i}\right) - \alpha\bar{u}_i + \frac{\partial \bar{p}}{\partial x_i} = 0 \tag{1a}$$

$$h_\mathrm{f}\frac{\partial \bar{u}_i}{\partial x_i} + \bar{u}_i\frac{\partial h_\mathrm{f}}{\partial x_i} = 0 \tag{1b}$$

where $i, j = 1, 2$; $\widetilde{\rho}_\mathrm{f} = \frac{5}{4}\rho_\mathrm{f}$, $\bar{\rho}_\mathrm{f} = \frac{6}{7}\rho_\mathrm{f}$ are the scaled densities, ρ_f is the density of the fluid; $\bar{u}$ is the velocity of the fluid in the mid-plane ($x_3 = 0$) of the channel; μ is the dynamic viscosity of the fluid; $\bar{p} = \frac{5}{4}p$ is the in-plane scaled pressure field and p is the original pressure field; $\alpha = \frac{10\mu}{{h_\mathrm{f}}^2}$ is the out-of-plane viscous resistance factor; h_f is the spacing height of the channel. The resistance term, $-\alpha\bar{u}_i$, represents the resistance of the channel to fluid, first proposed by Borrvall and Petersson (2003). The height correction term for mass conservation, $\bar{u}_i\frac{\partial h_\mathrm{f}}{\partial x_i}$, is used to ensure mass conservation as the height varies, and this term was introduced by Alexandersen (2022). The transient term, $\widetilde{\rho}_\mathrm{f}\frac{\partial \bar{u}_i}{\partial t}$, extends the previous steady-state problem to transient and was first proposed by Sun et al (2023). The derivation of the above parameters, except the transient term, can be found in (Alexandersen, 2022). The coefficients of the transient term are derived in the same way as the pressure term. To keep the present paper concise, it will not be repeated in this paper.

2.2 Reduced-dimensional model for heat transfer

This paper extends the previous reduced-dimensional model (Sun et al, 2022) to transient conjugate heat transfer and introduces the temperature field of the solid plates through the heat flux balance between the fluid and the solid on the contact surface. The temperature fields are governed by the convection-diffusion equation and the heat conduction equation, respectively, which are formulated as follows:
For fluid:

$$\rho_\mathrm{f}C_\mathrm{f}\frac{\partial T_\mathrm{f}}{\partial t} + \rho_\mathrm{f}C_\mathrm{f}u_i\frac{\partial T_\mathrm{f}}{\partial x_i} - \frac{\partial}{\partial x_i}\left(K_\mathrm{f}\frac{\partial T_\mathrm{f}}{\partial x_i}\right) = 0 \tag{2}$$

For solid:

$$\rho_s C_\mathrm{s}\frac{\partial T_\mathrm{s}}{\partial t} - \frac{\partial}{\partial x_i}\left(K_\mathrm{s}\frac{\partial T_\mathrm{s}}{\partial x_i}\right) - Q = 0 \tag{3}$$

where T_f and T_s are the temperature fields of the fluid and the solid, respectively; Q is the uniformly distributed heat source within the solid; C_f and C_s are the heat capacities of the fluid and the solid; K_f and K_s are the thermal conductivity of fluid and solid; and ρ_s is the density of solid. All these material properties are assumed to be independent of temperature. The temperature profile of the fluid is assumed to be a fourth-order polynomial (see argumentation by Yan et al (2019); Sun et al (2022)) and the temperature profile within the solid is assumed to be parabolic (the analytical solution through a solid wall with heat generation) as follows:

$$T_\mathrm{f}(x_1, x_2, x_3) = \bar{T}_\mathrm{f}(x_1, x_2) + \frac{\left(\left(\frac{2x_3}{h_\mathrm{f}}\right)^4 - 6\left(\frac{2x_3}{h_\mathrm{f}}\right)^2\right)}{5}\left(\bar{T}_\mathrm{f} - \bar{T}_\mathrm{i}\right) \tag{4a}$$

$$T_\mathrm{s}(x_1, x_2, x_3) = \bar{T}_\mathrm{s}(x_1, x_2) - \left(\frac{2x_3}{h_\mathrm{s}}\right)^2\left(\bar{T}_\mathrm{s} - \bar{T}_\mathrm{i}\right) \tag{4b}$$

where $\bar{T}_\mathrm{f}$ is the planar temperature field of the fluid in the mid-plane of the channel, $\bar{T}_\mathrm{s}$ is the planar temperature field in the mid-plane of the solid plate, $\bar{T}_\mathrm{i}$ is the temperature field at the fluid-solid contact interface, and h_s is the thickness of the solid plate. Similar to the derivation for fluid flow, the reduced-dimensional model for heat transfer can be derived by substituting the temperature profiles into the heat transfer equations, integrating over the thickness direction, and simplifying. A detailed derivation of the reduced-dimensional model for steady-state convective heat transfer is given in (Sun et al, 2022). This work extends it to the transient heat transfer process using the same methodology and the final reduced-dimensional model is as follows:

$$\begin{aligned}\rho_\mathrm{f} C_\mathrm{f}\left(\frac{\partial}{\partial t}\left(\bar{T}_\mathrm{f}+\tfrac{9}{16}\bar{T}_\mathrm{i}\right)+\frac{\partial}{\partial x_i}\left(\bar{u}_i h_\mathrm{f}\left(\tfrac{17}{21}\bar{T}_\mathrm{f}+\tfrac{13}{56}\bar{T}_\mathrm{i}\right)\right)\right)\\ -K_\mathrm{f}\frac{\partial}{\partial x_i}\left(\frac{\partial h_\mathrm{f}}{\partial x_i}\left(\bar{T}_\mathrm{f}-\bar{T}_\mathrm{i}\right)+h_\mathrm{f}\frac{\partial}{\partial x_i}\left(\bar{T}_\mathrm{f}+\tfrac{9}{16}\bar{T}_\mathrm{i}\right)\right)\\ +10K_\mathrm{f}\left(\frac{\bar{T}_\mathrm{f}-\bar{T}_\mathrm{i}}{h_\mathrm{f}}\right)=0\end{aligned} \tag{5}$$

The detailed derivation of the reduced-dimensional model for solid transient heat conduction is presented in Appendix A and the result is as follows:

$$\begin{aligned}\rho_\mathrm{s} C_\mathrm{s} h_\mathrm{s}\left(2\frac{\partial \bar{T}_\mathrm{s}}{\partial t}+\frac{\partial \bar{T}_\mathrm{i}}{\partial t}\right)+24K_\mathrm{s}\left(\frac{\bar{T}_\mathrm{s}-\bar{T}_\mathrm{i}}{h_\mathrm{s}}\right)-3Qh_\mathrm{s}\\ -K_\mathrm{s}\frac{\partial}{\partial x_i}\left(2\frac{\partial h_\mathrm{s}}{\partial x_i}\left(\bar{T}_\mathrm{s}-\bar{T}_\mathrm{i}\right)+h_\mathrm{s}\frac{\partial}{\partial x_i}\left(2\bar{T}_\mathrm{s}+\bar{T}_\mathrm{i}\right)\right)=0\end{aligned} \tag{6}$$

In the reduced-dimensional model described above, the temperature fields $\bar{T}_\mathrm{s}$ at the mid-plane of the solid plate, $\bar{T}_\mathrm{f}$ at the mid-plane of the fluid channel, and $\bar{T}_\mathrm{i}$ at the coupling interface are all the field variables to be solved. Therefore, additional heat flux balance equations need to be introduced to make the problem solvable. For this model, the heat flux balance equation for the fluid and solid at the coupling interface is formulated as follows:

$$-K_\mathrm{s}\left.\frac{\partial T_\mathrm{s}}{\partial x_3}\right|_{x_3=-\frac{h_\mathrm{s}}{2}}-K_\mathrm{f}\left.\frac{\partial T_\mathrm{f}}{\partial x_3}\right|_{x_3=\frac{h_\mathrm{f}}{2}}=0 \tag{7}$$

By substituting the temperature profile functions of the fluid and the solid, the final heat flux balance equation is as follows:

$$5K_\mathrm{s}\frac{\left(\bar{T}_\mathrm{s}-\bar{T}_\mathrm{i}\right)}{h_\mathrm{s}}+4K_\mathrm{f}\frac{\left(\bar{T}_\mathrm{f}-\bar{T}_\mathrm{i}\right)}{h_\mathrm{f}}=0 \tag{8}$$

The reduced-dimensional model for transient heat transfer with heat source plates and fluid channels is combined by Eq. 1,5,6,8

3 Model verification

This section takes the simplified symmetric model shown in Fig. 2 as an example and compares the results of the reduced-dimensional model with a full three-dimensional model to verify the accuracy of the proposed reduced-dimensional model for transient conjugate heat transfer.

3.1 Example description

The dimensions and boundaries of the selected symmetric model are shown in Fig. 3. In order to reduce the computational cost of simulation using the three-dimensional model, the three-dimensional geometry was modelled with only 1/4 of the symmetric model. The plate generates heat with a constant power P, which is uniformly distributed within the plate in the form of a volumetric heat source $Q = P/V$ - the implementation details are given in Appendix C. A fluid with a temperature T_in flows into the channel from the inlet, exchanges heat with the plate, and exits through the outlet. The internal fluid flow is driven an applied pressure drop between the inlet and the outlet, $\Delta p = p_\mathrm{in} - p_\mathrm{out}$. The side lengths of the plate and channel are L, the side lengths of the inlet and outlet of the channel are L_in, the maximum height of the channel is h_max, the minimum height of the channel is h_min, and the minimum thickness of the plate is h_bas. The height dimension of the model is much smaller than the dimension of its plane. Figure 3 also illustrates the height distribution of the contact surfaces of the channels and plates, where there are 6×6 circular dimples on the surface, which is an approximation of the common configuration of a pillow plate heat exchanger (Tong et al, 2022).

Figure 4 shows the boundary conditions and the model dimensions for the reduced-dimensional

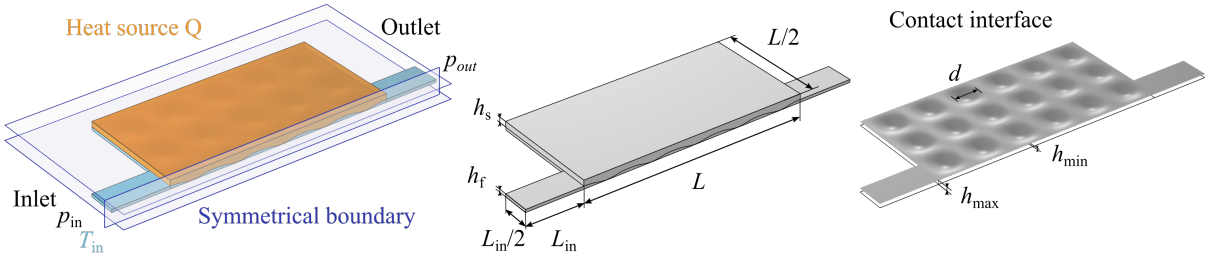

Fig. 3: Schematic diagram of the heat exchanger plate for full three-dimensional model verification with its dimensions and boundary conditions.

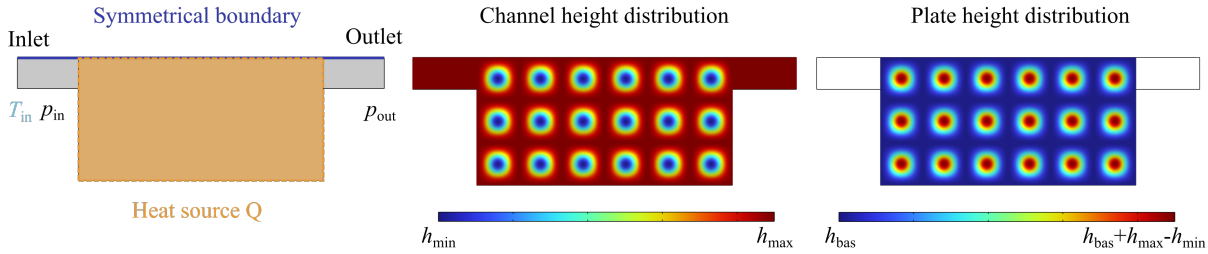

Fig. 4: Schematic diagram of the heat exchanger plate for reduced-dimensional model verification with its boundary conditions and height distribution.

model. The reduced-dimensional models for both fluids and solids are defined at the mid-plane of the channel ($x_3 = 0$), and the reduced-dimensional model for solids sets $Q = 0$ for the heat source in the inlet and outlet regions. The dimensions and material properties of the model are shown in Table 1.

3.2 Simulation details

All the simulations carried out in this section are completed in COMSOL Multiphysics Version 6.0 (COMSOL, 2022). The full three-dimensional model simulation is implemented using the "Laminar Flow" interface and the "Heat Transfer in Fluids and Solids" interface; the reduced-dimensional model is implemented using the "Weak Form Boundary PDE" interface. Second-order shape functions are used to discretise the velocity field combined with first-order shape functions for the pressure field to yield a stable system. The temperature field is discretised using first-order shape functions. The meshes used for the simulations and their convergence analysis are shown in Appendix B.

Table 1: Parameters for the verification example

Parameters	Symbols	Values	Units
Length of plate	L	150	mm
Length of inlet	L_{in}	37.5	mm
Minimum channel height	h_{min}	0.5	mm
Maximum channel height	h_{max}	2.5	mm
Base thickness of plate	h_{bas}	2.5	mm
Diameter of dimple	d	16.6	mm
Initial temperature	T_{int}	293.15	K
Inlet temperature	T_{in}	293.15	K
Total power	P	150	W
Pressure drop	Δp	30	Pa
Density of solids	ρ_{s}	8000	kg/mˆ3
Density of fluids	ρ_{f}	1064	kg/mˆ3
Heat conductivity of solids	K_{s}	0.394	W/(m·K)
Heat conductivity of fluids	K_{f}	16.3	W/(m·K)
Heat capacity of solids	C_{s}	500	J/(kg·K)
Heat capacity of fluids	C_{f}	3358	J/(kg·K)
Viscosity of fluids	μ	0.0023	Pa·s

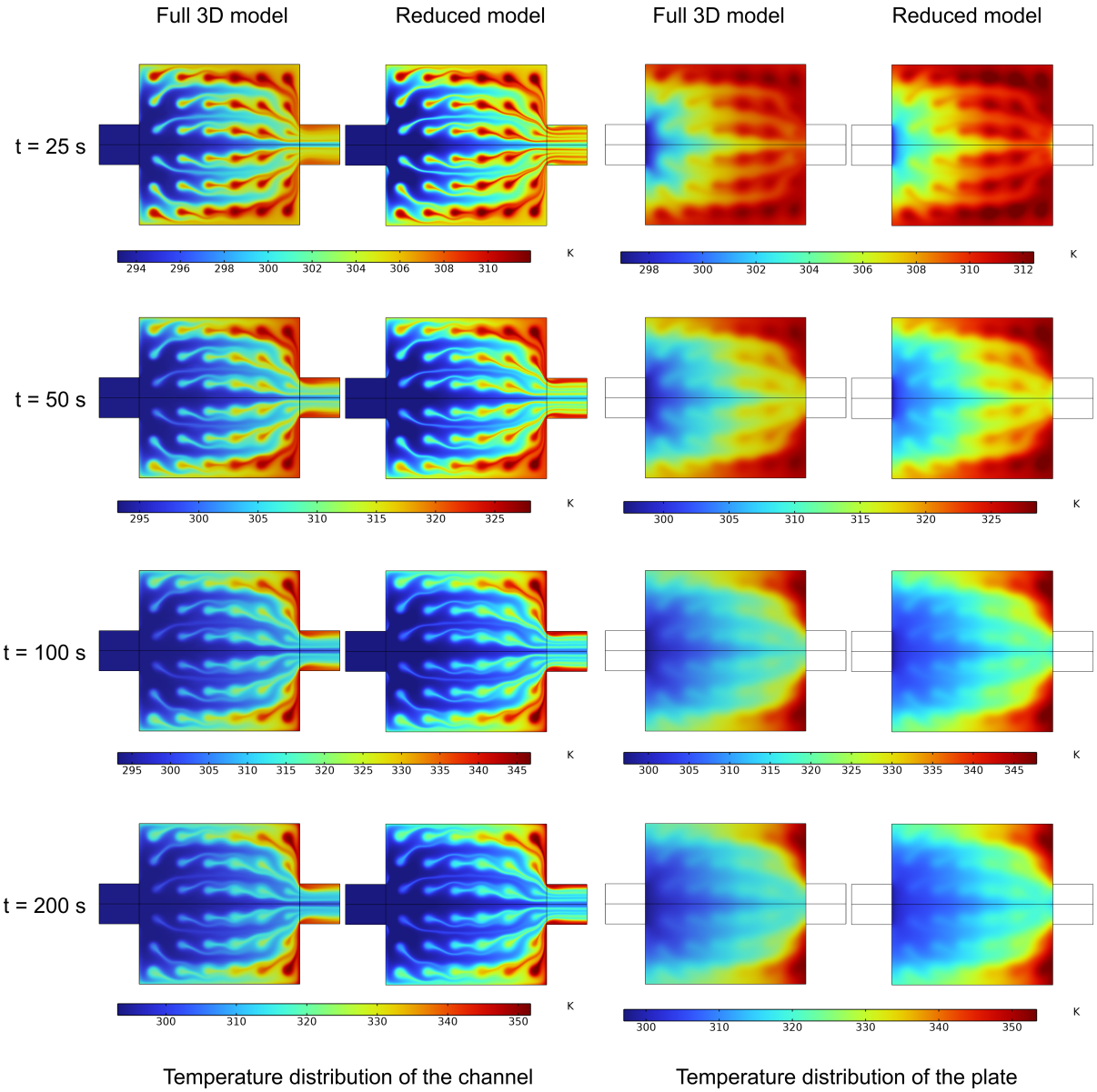

Fig. 5: Comparison of temperature at different moments between the reduced-dimensional model and the full three-dimensional model. Please note that the colour scale varies from column to column to allow details of the distribution to be clear.

This section simulates the transient temperature distribution of the channel and plate over [0, 200] s. The relative tolerance of the solvers is set to 10^{-3}. The Backward Differentiation Formula (BDF) implementation in COMSOL is used as the time stepping approach, with a maximum BDF order of 2, a fixed time step of 2 s, an initial step factor of 0.01 and a growth rate of 1.5. Separate solvers are used for both the full and reduced-dimensional models. Since the material properties are independent of temperature, the flow field can be solved first and thereafter the temperature field in a sequential fashion.

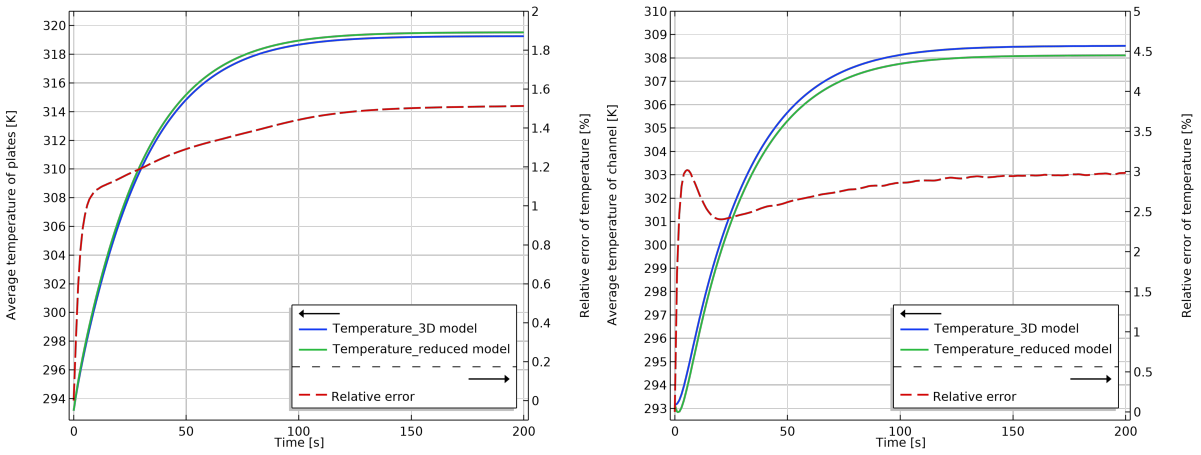

(a) Average temperature of the plates and the relative error.

(b) Average temperature of the channel and the relative error.

Fig. 6: Average temperature and relative error in temperature of the channels and plates obtained using the reduced and full models in continuous time.

Table 2: Time-accumulated temperature error between full model and reduced-dimensional model.

Area	Average temperature over time [K]		Average relative error
	Reduced model	Full model	over time [%]
Plate	315.62	315.91	1.37
Channel	306.17	305.77	2.79

3.3 Comparison with full model

Figure 5 shows the temperature distribution in the mid-plane of the channel and the plate at different moments using the full three-dimensional model and the reduced-dimensional model. It can be observed that the temperature distributions obtained using the reduced-dimensional model are in good agreement with the results obtained using the full model. The reduced-dimensional model accurately simulates the temperature distribution of the fluid and solid within and behind the dimple region. This shows that the reduced-dimensional model can represent the effect of topography variations at the coupled interface on the heat exchange between the channel and the plate very well.

In order to quantify the agreement of the temperature between the reduced-dimensional model and the full three-dimensional model, the spatially-averaged relative error is defined as:

$$e_{\mathrm{s}}^{t_i} = \frac{1}{|\omega_{\mathrm{s}}|} \int_{\omega_{\mathrm{s}}} \frac{|\bar{T}_{\mathrm{s}}^{3D} - \bar{T}_{\mathrm{s}}^{2D}|}{\bar{T}_{\mathrm{s}}^{3D} - T_{\mathrm{ref}}} \, dS \, |_{t=t_i} \tag{9}$$

$$e_{\mathrm{f}}^{t_i} = \frac{1}{|\omega_{\mathrm{f}}|} \int_{\omega_{\mathrm{f}}} \frac{|\bar{T}_{\mathrm{f}}^{3D} - \bar{T}_{\mathrm{f}}^{2D}|}{\bar{T}_{\mathrm{f}}^{3D} - T_{\mathrm{ref}}} \, dS \, |_{t=t_i} \tag{10}$$

where $e_{\mathrm{s}}^{t_i}$ and $e_{\mathrm{f}}^{t_i}$ represent the spatially-averaged relative error of the solid and fluid at time $t = t_i$, respectively; ω_{s} and ω_{f} are the mid-planes defined inside the plate and channel, respectively; $\bar{T}_{\mathrm{s}}^{3D}$ and $\bar{T}_{\mathrm{s}}^{2D}$ are the solid temperatures of the plane at that moment, calculated using the full model and the reduced-dimensional model, respectively; $\bar{T}_{\mathrm{f}}^{3D}$ and $\bar{T}_{\mathrm{f}}^{2D}$ are the fluid temperatures of the plane calculated using the full model and the reduced-dimensional model, respectively; T_{ref} is the reference temperature. The time-averaged relative error of the two models for the entire time

can be expressed by the following equation:

$$e_{\mathrm{s}}^{int} = \frac{1}{|t-t_0|}\int_{t_0}^{t} e_{\mathrm{f}}^{t_i}\ dt \tag{11}$$

$$e_{\mathrm{f}}^{int} = \frac{1}{|t-t_0|}\int_{t_0}^{t} e_{\mathrm{f}}^{t_i}\ dt \tag{12}$$

where e_{s}^{int} and e_{f}^{int} denote the time-averaged relative error over the entire time period for solids and fluids, respectively; t_0 is the initial time and t is the final time.

Figure 6 shows the spatially-averaged relative error for the temperature of the solid and the fluid over time. The solid line shows the variation of the average temperature and the dashed line shows the average relative error between the two models. The graph shows that the average temperature of the fluid and solid obtained from the reduced-dimensional model follows the same trend as the three-dimensional model and are generally very close. As can be seen from the dashed line, the results of the two models are in good agreement. The error regarding the plate temperature increases rapidly in the initial phase and remains constant after the temperature reaches steady state, with an error of less than 1.6%; the error regarding the fluid temperature in the channel also varies in much the same way, with an final error of about 3%. The time-averaged temperature and relative error between the plate and the channel in the range $t \in [0, 200]$s are shown in Table 2. The average error about time for both the plate and the channel obtained by the two models is within 3%, and it can be assumed that the reduced-dimensional model can be used to simplify the transient temperature analysis of the structure with the complex topography.

4 Optimisation formulation

This section presents the formulation of the optimisation of the heat exchanger plate and the implementation of the reduced-dimensional model in combination with topography optimisation.

4.1 Design parametrisation

This work optimises a heat exchanger plate, as shown in Fig. 2, by varying the topography of the heated plate, and thus the height of the fluid channel, to enhance heat transfer. In the optimisation process, the topography is represented by a height field defined at each node. The design variable field γ is introduced to couple with the height field to enable iterative optimisation and updating of the structure during the optimisation process. A linear interpolation scheme is used to define the local height of the channel and the thickness of the plate as follows:

$$\begin{aligned} h_{\mathrm{f}}(x_1, x_2) &= h_{\min} + (h_{\max} - h_{\min})\,\gamma(x_1, x_2) \\ h_{\mathrm{s}}(x_1, x_2) &= h_{\mathrm{bas}} + h_{\max} - h_{\mathrm{f}}(x_1, x_2) \end{aligned} \tag{13}$$

where h_{f} is the height of the channel, h_{s} is the thickness of the heat exchanger plate, $h_{\min}$ and $h_{\max}$ are the lower and upper limits of the channel height, h_{bas} is the base thickness of the heat exchanger plate, and γ is a continuous design variable field $\gamma \in [0, 1]$. When $\gamma = 0$, the height of the channel at this point reaches the lower limit $h_f = h_{\min}$, and the thickness of the heat exchanger plate reaches the upper limit $h_{\mathrm{s}} = h_{\mathrm{bas}} + h_{\max} - h_{\min}$. When $h_{\min} = 0$, it can be considered that the upper and lower surfaces of the channel are in contact at this point and the channel is blocked at this point, i.e., the topology of the channel changes. When $h_{\min} > 0$, the topology of the structure does not change and the topographic variation takes place in the structure.

When $\gamma = 1$, the height of the channel at this point reaches the upper limit $h_{\mathrm{f}} = h_{\max}$ and the thickness of the heat exchanger plate is the basic plate thickness $h_{\mathrm{s}} = h_{\mathrm{bas}}$. When $\gamma \in]0, 1[$ holds intermediate values, the height and thickness are obtained by the Eq. 13. The height-based interpolation scheme above has the advantage that intermediate design variables naturally have a physical meaning. Therefore, penalisation, projection and other methods to ensure discrete 0-1 designs, as in topology optimisation, is not necessary. Furthermore, the implicit definition of the fluid-solid contact interface is avoided, since the fluid-solid contact interface always exists analytically on the surface of a continuous channel controlled by h_{f} and h_{s}, which can be expressed as an isosurface with $x_3 = h_{\mathrm{f}}$.

4.2 Optimisation formulation

In this work, a single heat exchanger plate from a plate-type heat exchanger, as shown in Fig. 2, is optimised for better heat transfer performance

at a constant pressure drop. The entire heat exchanger plate area is chosen as the design domain, and the extended area of the inlet and outlet is the non-design area. The optimisation area and its initial conditions are shown in Fig. 7. The dimensional parameters and material properties of the heat exchanger plate and adjacent flow channels are the same as in the previous sections, see Table 1. During the optimisation process, the channel height is optimised in the range of $h_{\mathrm{f}} \in [h_{\min}, h_{\max}]$.

The temperature of the heat exchanger plate is one of the most intuitive measures of the heat transfer efficiency of the structure, by minimising the plate temperature, the heat transfer performance of the overall system can be maximised. This work takes the spatially-averaged temperature of the heat exchanger plate as the optimisation objective ϕ, which is established as follows:

$$\phi = \frac{1}{V_{\mathrm{s}}} \int_{\Omega_{\mathrm{s}}} T_{\mathrm{s}} \ dV \tag{14}$$

where Ω_{s} is the area of the heat exchanger plate in three dimensions and V_{s} is the volume of the area of the heat exchanger plate in three dimensions. By substituting the temperature profile function of the solid, the above optimisation objective can be further expressed as:

$$\phi = \frac{1}{S_{\mathrm{s}}} \int_{\omega_{\mathrm{s}}} \frac{2}{3}\bar{T}_{\mathrm{s}} + \frac{1}{3}\bar{T}_{\mathrm{i}} \ dS \tag{15}$$

where ω_{s} is the heat exchanger plate domain and S_{s} is the surface area of the heat exchanger plate in reduced model. This work performs optimisation in the steady-state and transient-states, respectively. The steady-state optimisation problem is established as follows:

$$\begin{aligned} \underset{\gamma}{\text{Minimise:}} \quad & \phi \,|_{\text{steady-state}} \\ \text{Subject to:} \quad & 0 \leq \gamma \leq 1 \\ & \text{Reduced model}\,(Eq.\ 1, 5, 6, 8) \end{aligned} \tag{16}$$

The steady-state optimisation described above ignores the process of temperature variation with time and focuses only on the heat transfer performance once the temperature has reached steady-state by ignoring the time derivative terms in the governing equations, which can save the computational source for optimisation. This is applicable to the ideal case where the heat exchange time is sufficiently long, but there are certain practical engineering scenarios where the operating time of the heat exchanger is limited. The heat exchanger might need to exchange heat in a relatively short time or react fastly, and the process of temperature variation takes up the majority of its operating time. Therefore, the variation of temperature with time cannot be neglected and the optimisation of the heat exchanger structure needs to be performed in the transient framework, with the optimisation problem established as follows:

$$\begin{aligned} \underset{\gamma}{\text{Minimise:}} \quad & \phi \,|_{t=t_{\text{end}}} \\ \text{Subject to:} \quad & 0 \leq \gamma \leq 1 \\ & \text{Reduced model}\,(Eq.\ 1, 5, 6, 8) \end{aligned} \tag{17}$$

This objective is to minimise the spatially-averaged temperature of the heat exchange plate at final time $t = t_{\text{end}}$. It is worth stating that the power of the heat source is constant over time and, thus, the temperature of the plate increases monotonically. Taking the temperature integral over time as the objective and taking the temperature at the final time $t = t_{\text{end}}$ as the objective yields optimised designs that are almost identical in structure as well as performance; this work takes the temperature at the final time as the objective for transient optimisation.

4.3 Implementation

To avoid possible numerical problems in the optimisation process, a Helmholtz-type PDE filter (Lazarov and Sigmund, 2011) is introduced to regularise the optimisation problem and to control the gradient of height variation of the channels and plates during the optimisation process, avoiding errors in the reduced-dimensional model caused by features with drastic height variation in the optimised design as previously shown by Alexandersen (2022) and Sun et al (2022). The PDE filter is applied to the fluid height directly as follows:

$$-r^2\nabla^2 h_{\mathrm{f}} + h_{\mathrm{f}} = \bar{h}_{\mathrm{f}} \tag{18}$$

where $r = \frac{r_{\min}}{2\sqrt{3}}$, r is the filter parameter; $r_{\min}$ is the filter radii, the size of which is related to the

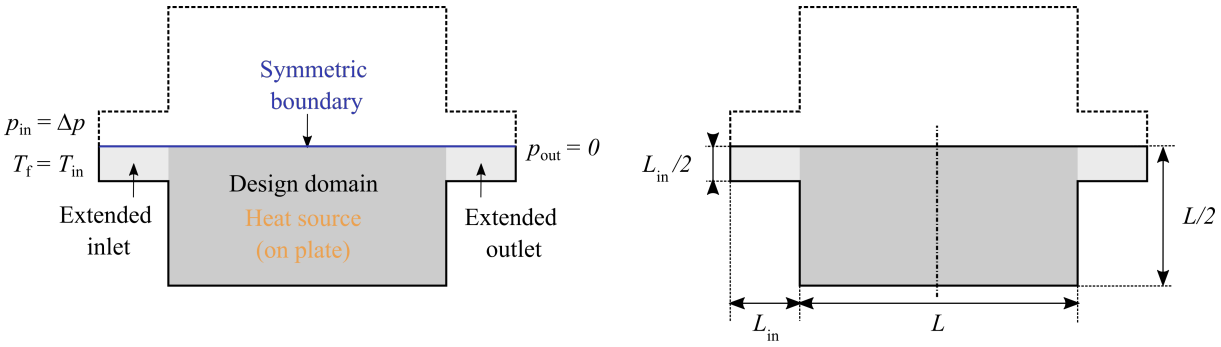

(a) Boundary conditions (b) Dimensions

Fig. 7: Domains and boundary conditions for optimisation.

maximum height gradient; $\bar{h}_f$ is the height distribution defined by Eq. 13 and h_f is the continuous height field obtained after the filter.

The optimisation in this work are carried out completely within COMSOL Multiphysics Version 6.0 (COMSOL, 2022). The construction of the design variable fields and the implementation of the corresponding interpolation schemes are completed using the optimisation module. The reduced-dimensional model is implemented using "Weak Form PDE" interface. The filtering is implemented via the "Coefficient Form PDE" interface. The adjoint sensitivities of the optimisation objective to the design variables are obtained using the automatic differentiation method built into COMSOL, and the sensitivities in the transient optimisation are solved by backward time stepping. MMA is used to solve the optimisation problem, where the move limit of the updated design variables is 0.2.

5 Optimisation results

5.1 Steady optimisation

This section presents the results of the steady-state topography optimisation of the heat exchanger plate and analyses their implications for heat transfer performance. The mesh for the optimisation consists of quadrilaterals with a length of L/250, chosen as a balance between accuracy and computational time. The filter radii r_{min} in the PDE filter is defined as L/30, which is large enough to ensure that the height variation during the optimisation process is moderate and no additional errors are induced. The maximum number of optimisation iterations is set to 300.

5.1.1 Varying the applied pressure drop

The applied pressure drop between the inlet and outlet of the channel is a critical parameter in the optimisation process and can significantly affect the resulting design. This section aims to investigate the impact of different pressure drops on the optimisation results for the heat exchanger plate. Figure 8 displays the optimised designs obtained for applied pressure drops of 20, 30, 50, and 75 Pa, and Fig. 9 shows their corresponding velocity and temperature distributions.

It can be seen that the basic layout of the height distribution is the same for the optimised designs obtained at different pressure drops. When $\Delta p = 20$ Pa, there is no areas of minimum channel height in the optimised design and the topography only contains intermediate heights. As Δp increases, the area with intermediate heights in the optimised design decreases, while the area with minimum heights increases. For the velocity distribution, when Δp increases, more areas of low height appears, increasing the resistance to flow. As a result, the velocity of the fluid in this area decreases, and the fluid will bypass the area of topography variation, resulting in an increase in velocity around this area. However, it should be noted that even in the area of minimum height, the fluid still passes through, so the minimum velocity is not zero. For the temperature distribution, the higher the pressure drop, the lower the fluid and solid temperatures for the corresponding optimised design. This is due to the fact that the increased pressure drop allows the optimisation algorithm to produce optimised designs with more complex topography, which have a larger contact

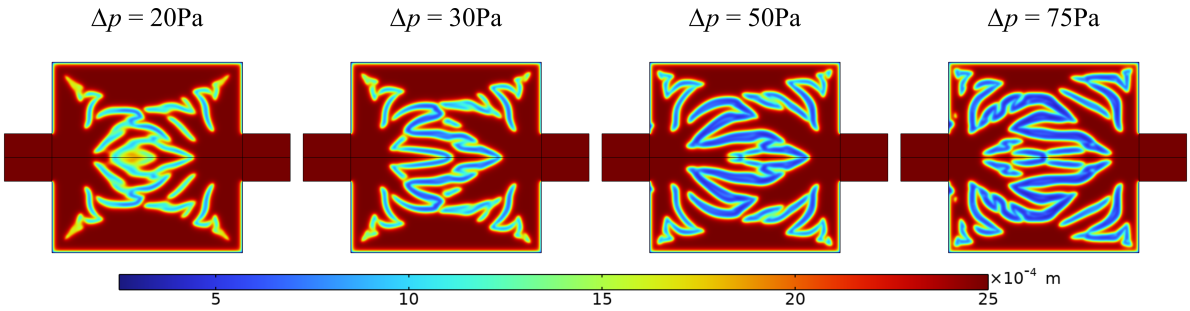

(a) Optimised height distribution of channel

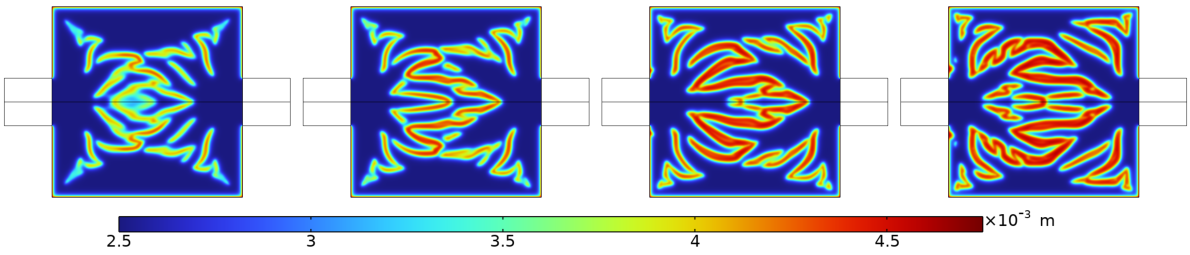

(b) Optimised height distribution of plate

Fig. 8: Height distribution of the optimised design with different pressure drop.

Table 3: Cross-check results of different optimised designs at different pressure drops.

Pressure drop [Pa]	Reference design	Temperature of optimised design with different Δp			
		$\Delta p = 20$	$\Delta p = 30$	$\Delta p = 50$	$\Delta p = 75$
20	326.99	**320.60**	320.69	321.97	324.25
30	319.42	314.68	**314.42**	314.73	315.90
50	313.32	310.09	309.57	**309.13**	309.33
75	310.19	308.02	307.32	306.52	**306.21**

area with the fluid and better heat exchange performance. In addition, the increased pressure drop results in a greater velocity of the internal fluid, which has a stronger convective effect, leading to a lower overall temperature.

In order to verify the performance of the above optimised designs, this section reanalyses the reference design and the above optimised designs on a finer mesh at pressure drops of 20, 30, 50, and 75 Pa, respectively, with the corresponding average temperatures for each design shown in the Table 3. It can be seen that the average temperature of the plates for the optimised design is significantly lower than that of the reference design at all pressure drops. For the same pressure drop, the average plate temperature of the optimised design can even be 6 K lower than that of the reference design. Furthermore, for each of the different optimised designs, the lowest temperatures were obtained at the pressure drop used in their optimisation, i.e., the best heat transfer performance. Thus, the effectiveness of the optimisation was verified.

5.1.2 Verification using three-dimensional model

In order to verify that the performance of the actual three-dimensional structure generated from the optimised designs is consistent with the predictions, this section generates the corresponding three-dimensional design based on the optimisation results from the previous section and reanalyses them using the full model, comparing

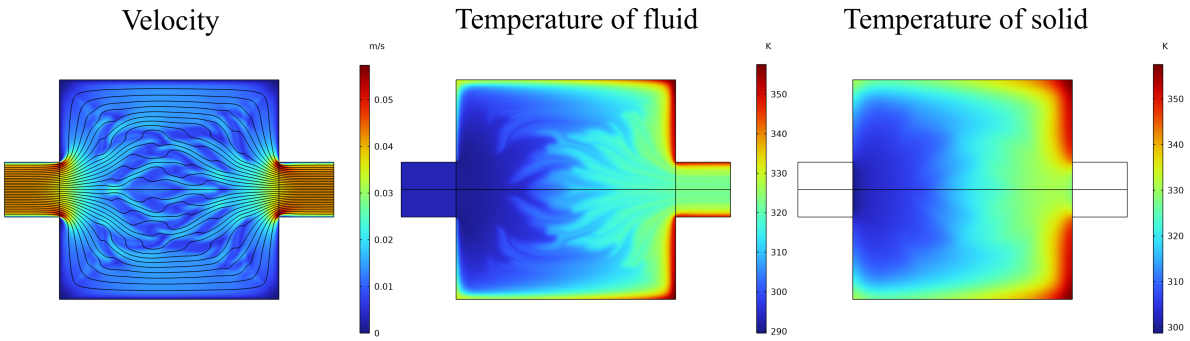

(a) Optimised design for $\Delta p = 20$Pa

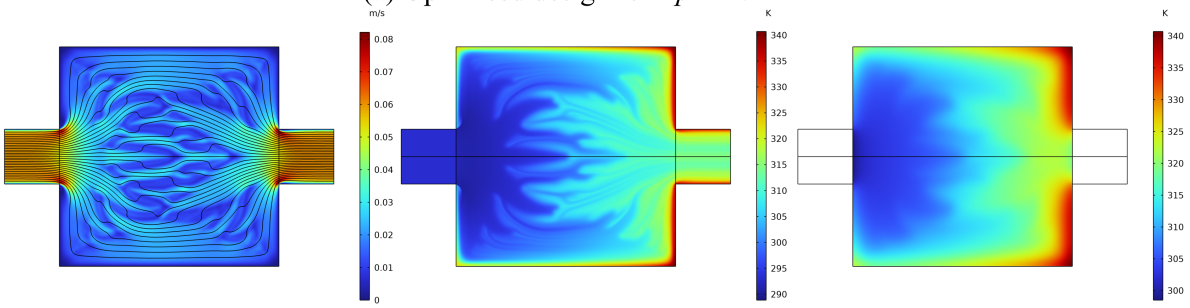

(b) Optimised design for $\Delta p = 30$Pa

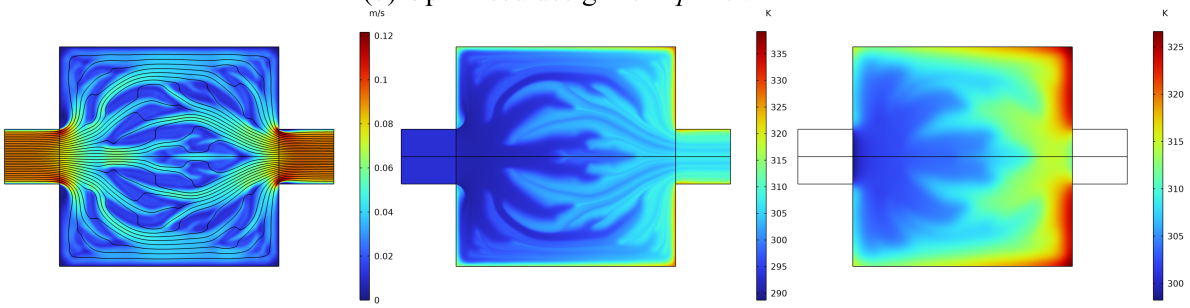

(c) Optimised design for $\Delta p = 50$Pa

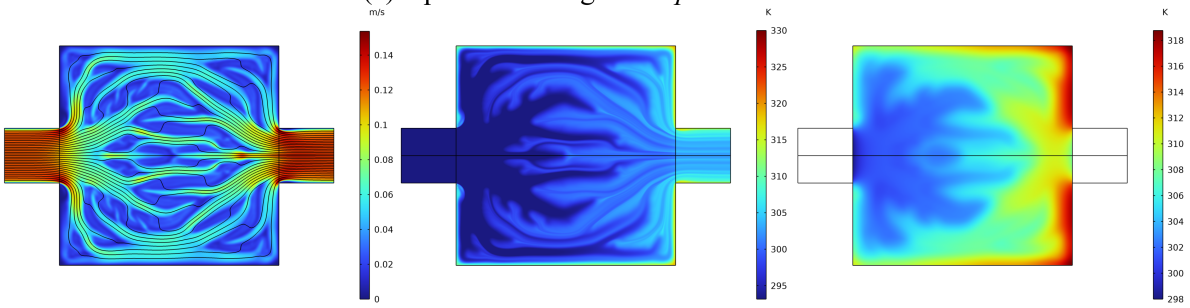

(d) Optimised design for $\Delta p = 75$Pa

Fig. 9: Velocity and temperature distribution of the optimised design with different pressure drop.

the results with those of the reduced-dimensional model. Figure 10 shows the generated three-dimensional geometry for the optimised designs.

All the generated three-dimensional models of the optimised design are evaluated at $\Delta p = 30$ Pa. The mesh used for the analysis is essentially the same as that used for the Section 3, which are obtained by mapping the plane using quadrilateral elements with an $L/125$ side length. The mesh consists of a total of 92,769 elements and

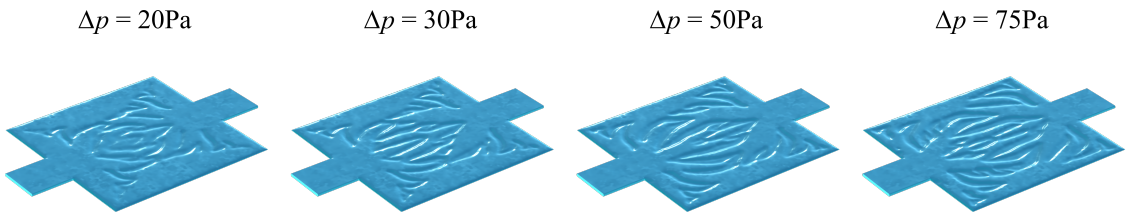

(a) Three-dimensional geometry of the optimised channel

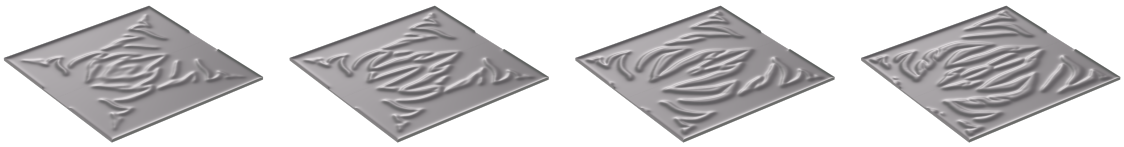

(b) Three-dimensional geometry of the optimised plate

Fig. 10: Three-dimensional geometry of plates and channels generated from different optimised designs.

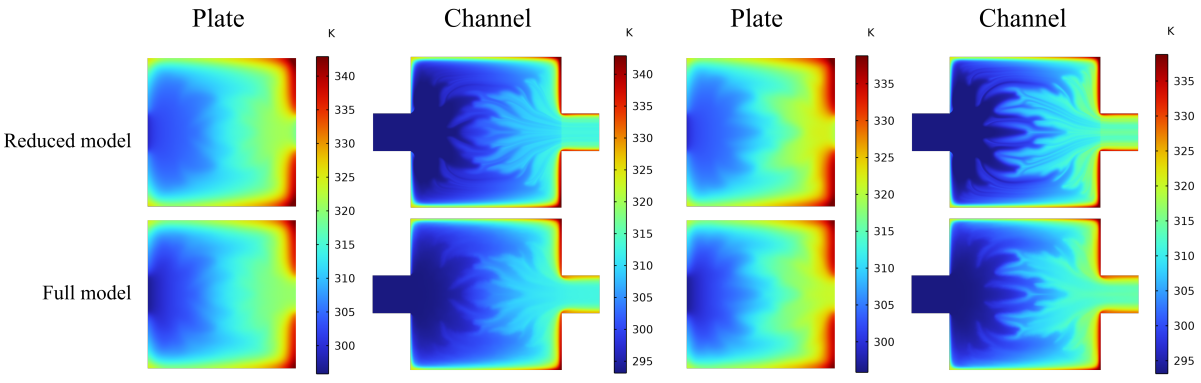

(a) Optimised design for $\Delta p = 20$Pa (b) Optimised design for $\Delta p = 30$Pa

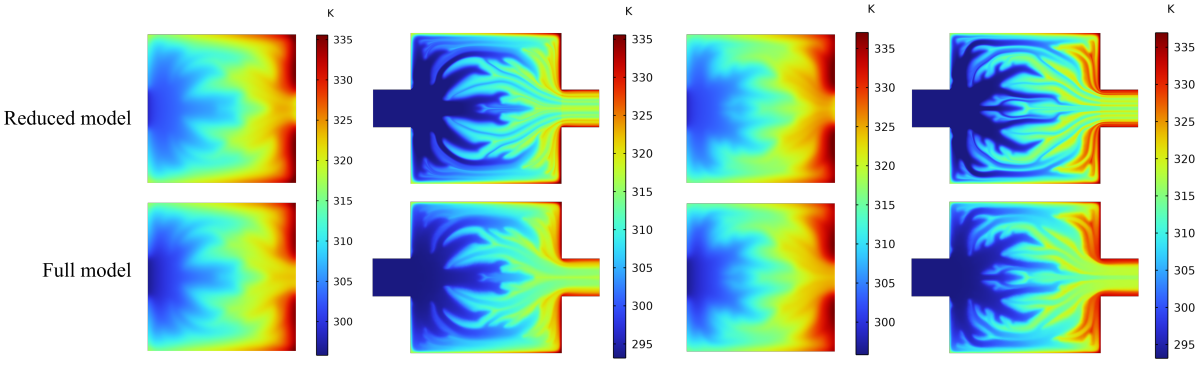

(c) Optimised design for $\Delta p = 50$Pa (d) Optimised design for $\Delta p = 75$Pa

Fig. 11: Comparison of temperatures obtained for different optimised designs using reduced-dimensional models and full three-dimensional models.

the number of degrees of freedom (DOFs) to be solved is 1,576,389. In the case of the design optimised at $\Delta p = 30$ Pa, the solution time is 2,753 s. It should be noted that when the same analysis is performed using the reduced-dimensional model with a finer mesh of side length $L/300$, the computation time is only 52 s. This is a significant reduction in computational time and highlights the main motivation for introducing the reduced-dimensional model.

Figure 11 shows the plate and channel temperature distributions for each design analysed using the full model and the reduced-dimensional model. It can be seen that for all the optimised designs, the temperatures obtained using the full model fit well with the results obtained using the reduced-dimensional model. In addition, the channel temperature distributions from the reduced-dimensional model have more detail due to the fact that the mesh used for the reduced-dimensional model is finer in plane than the mesh used for the full model.

Table 4 presents the average plate temperatures obtained using the full model for each optimised design at a pressure drop of 30 Pa. It can be observed that the temperatures obtained using the full model are in good agreement with the temperatures obtained using the reduced-dimensional model. Furthermore, the plate temperatures for each optimised design are lower than those for the reference design. Among the optimised designs obtained at different pressure drops, the design obtained at a pressure drop of 30 Pa has the lowest plate temperature in this verification, which confirms the effectiveness of the optimised design.

5.2 Transient optimisation

This section presents the results of applying the reduced-dimensional model to the transient optimisation of the plate heat exchanger, investigates the effect of different operating time on the optimisation results, and compares them with the results of the steady-state optimisation. The optimisation problem is formulated in Eq. 17. The pressure drop between the inlet and outlet in the channel is $\Delta p = 30$ Pa. To facilitate comparison with the results of the steady-state optimisation, all optimisation parameters in this section are set to be the same as those in the steady-state optimisation. However, due to the substantial increase in computational cost brought by the transient analysis, a coarser planar mesh of quadrilateral elements with a side length of $L/150$ is used for transient optimisation. For verification, a planar mesh of quadrilateral elements with side length of $L/300$ is used to compute the velocity and temperature distributions. All optimisations were performed using a constant time step of 2 seconds, which has been chosen based on time step convergence studies.

5.2.1 Varying the operating time

This section investigates the effect of different operating times, denoted as t_{end}, on the transient optimisation results. Figure 12 shows the optimised designs using the transient optimisation and the steady-state optimisation. It can be seen that the distribution of the optimised designs obtained at different t_{end} differs significantly, but the same main structural form is maintained for all optimised designs. When the t_{end} is relatively small, the channel area is small and mainly concentrated in the middle area between the channel inlet and outlet. As t_{end} increases, the area of the channel flow area increases and the distribution becomes more dispersed. Furthermore, as the t_{end} increases, the optimised structure tends to the steady-state design, which proves the reliability of the optimisation algorithm.

To further verify the reliability of the optimisation algorithm, this section analyses the above optimised designs with different t_{end} within the range of 0-200 seconds and compares the temperature performance of the different designs at different t_{end}. Figure 13 shows the variation of the spatially-averaged temperature of the plate for the above optimised designs over the entire time range. The plate temperature of each optimised design is lowest at its corresponding operating time t_{end}; when the time is long enough, the steady-state design has the lowest plate temperature, which proves the reliability of the optimisation results. It can also be observed that the steady-state design has the highest plate temperature in the short term, while for the designs with $t_{\text{end}} = 15$s and 20s, although they perform well in the short term, their temperature becomes significantly higher than the other designs when the time exceeds the specific t_{end}.

Table 4: Cross-check results of different optimised designs using full three-dimensional model.

Model	Reference design	Optimised design with different Δp			
		$\Delta p = 20$	$\Delta p = 30$	$\Delta p = 50$	$\Delta p = 75$
Reduced model	319.42	314.68	**314.42**	314.73	315.90
Full model	319.26	314.51	**314.22**	314.56	315.80

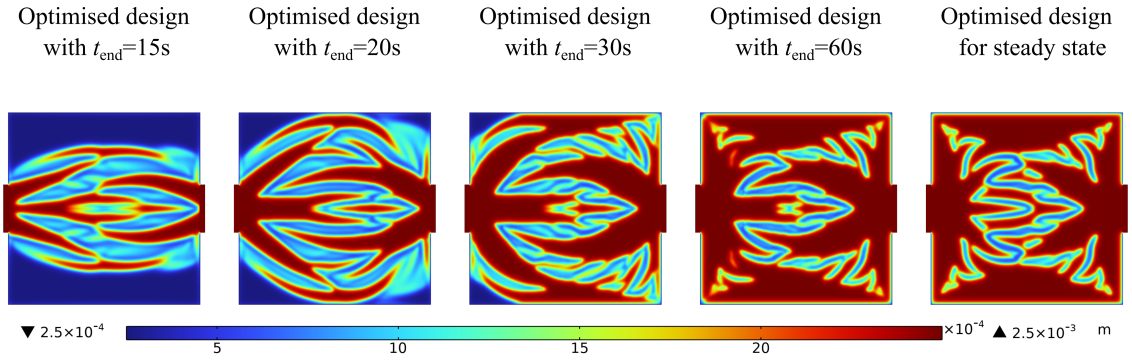

(a) Channel height

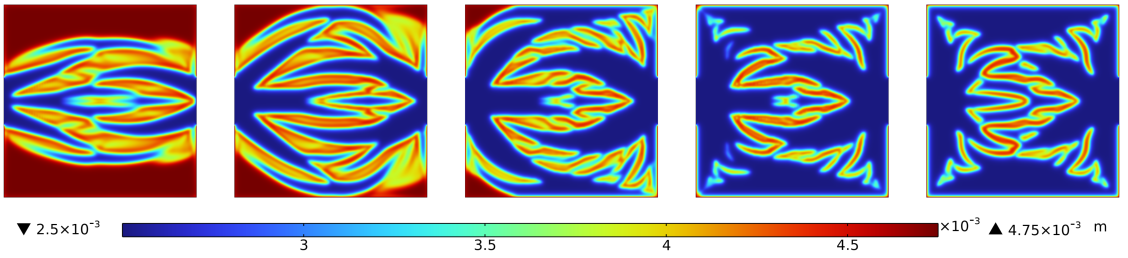

(b) Plate height

Fig. 12: Transient optimised designs obtained with different t_{end}.

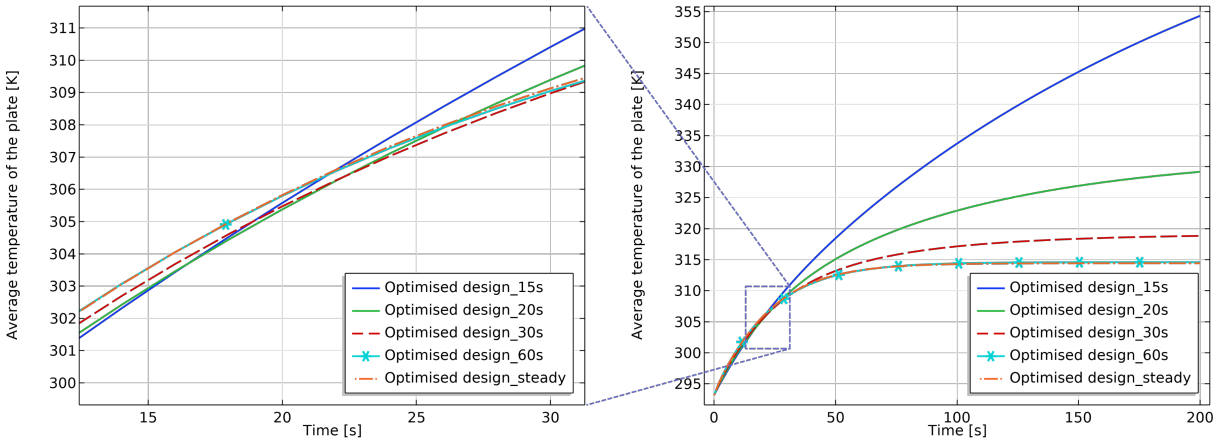

Fig. 13: Comparison of average plate temperatures at [0,200] s for different transient optimised designs.

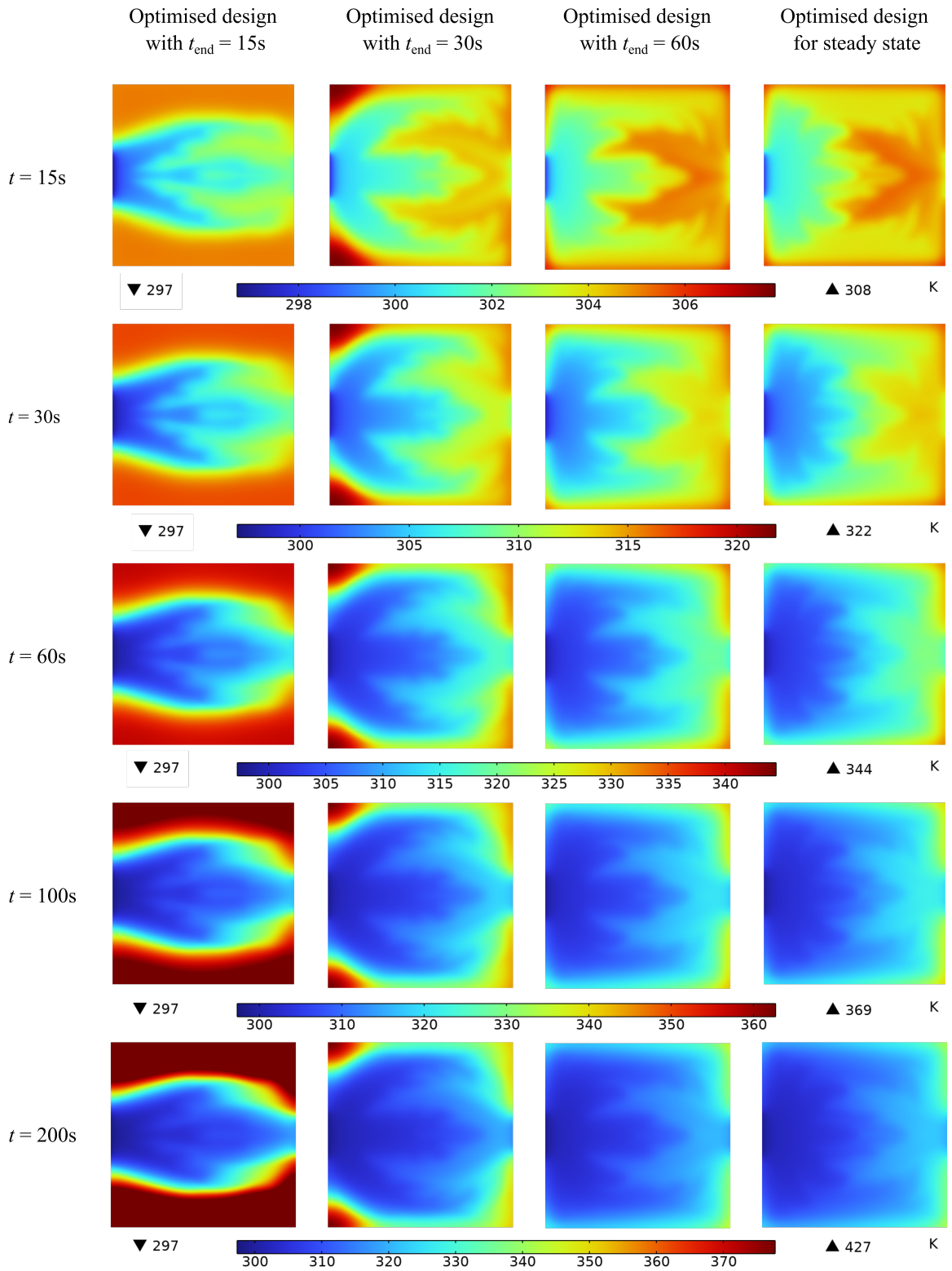

Fig. 14: Illustration of plate temperatures for three optimised designs at different times using reduced-dimensional model.

Table 5: Cross-check results of different optimised designs at different times.

Time[s]	Reference design	Optimised design with different tend				
		t=15s	t=20s	t=30s	t=60s	Steady state
15	303.91	**302.87**	302.94	303.19	303.56	303.56
20	306.40	305.58	**305.38**	305.47	305.79	305.82
30	310.33	310.41	309.39	**308.97**	309.05	309.13
60	316.50	321.93	317.18	314.46	**313.25**	313.28
100	318.88	333.71	322.90	317.14	314.40	**314.29**
150	319.40	345.27	326.90	318.37	314.58	**314.41**
200	319.46	354.30	329.16	318.84	314.59	**314.42**

To compare the heat transfer performance of the different designs, Table 5 shows the spatially-averaged plate temperature for the different designs at different times. The bold text indicates the lowest temperature at each time. It can be seen that the temperatures of the optimised designs are all significantly lower than the reference design at the corresponding objective times. Furthermore, when $t_{\text{end}} = 15$ s, the plate temperature of the transient optimised design can be about 1 K lower than the steady-state optimised design, but when the time reaches 200 s, the plate temperature of this design is about 40 K higher than the steady-state design. To intuitively understand the reason for the above phenomenon, Fig. 14 shows the plate temperature distribution of the optimised design at different times. It can be seen that the design with $t_{\text{end}} = 15$ s confines the fluid flow to the middle area of the channel by changing the topography of the plate, resulting in a stronger convective effect in that area and therefore a lower plate temperature. The steady-state design, on the other hand, has a more dispersed channel and weaker local convective effects, resulting in a higher temperature in the middle area in the short term. However, when the heat exchange time is long enough for the fluid to fully exchange heat with the plate and the steady-state design has more dispersed flow channels and a larger contact surface area, the overall average temperature is lower than in the transient design.

5.2.2 Verification using full model

In this section, the transient optimised design with t_{end}=15 s and t_{end}=30 s and the steady-state optimised design are chosen to be reconstructed into three-dimensional geometry and analysed to verify the reliability of applying the reduced-dimensional model to transient optimisation by comparing with the reference design. The three-dimensional geometry of the steady-state design and the reference design are shown in Fig. 3 and 10. The three-dimensional geometry of the optimised design with $t_{\text{end}} = 15$ s and $t_{\text{end}} = 30$ s is shown in Fig. 15.

The temperature variation of the selected transient optimised design and the steady-state optimised design is analysed in $t \in [0, 200]$s using a full three-dimensional model to verify the performance of the reconstructed three-dimensional geometry for the transient optimised design. The mesh for analysis uses the same mesh framework as the analysis example, using quadrilateral elements with side lengths of $L/125$ to discretize the plane, and the planar mesh is mapped to produce the three-dimensional mesh. The mesh consists of 100,644 elements, and the number of DOFs to be solved is 1,349,543. For the optimised design with $t_{\text{end}} = 30$ s, the solution time is 15,567 s. It should be noted that when using the reduced-dimensional model with a finer mesh of side length $L/300$, the solution time is only 556 s. This once more highlight the significant computational cost achieved by applying the reduced-dimensional model to topography optimisation of conjugate heat transfer in flow in gaps between heated plates.

Figure 16 shows the spatially-averaged temperature of the plate over time for the optimised design using the full model and the reduced-dimensional model, as well as the relative error between the two models. For the steady-state design and the transient design with $t_{\text{end}} = 30$ s, the temperature profiles obtained from the reduced-dimensional model fit well with the full model over time, and the relative errors are kept

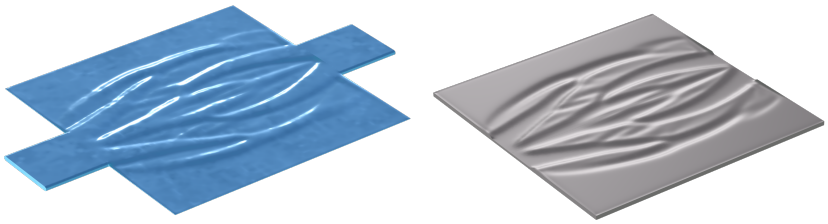

(a) Design optimised at t_{end}=15s

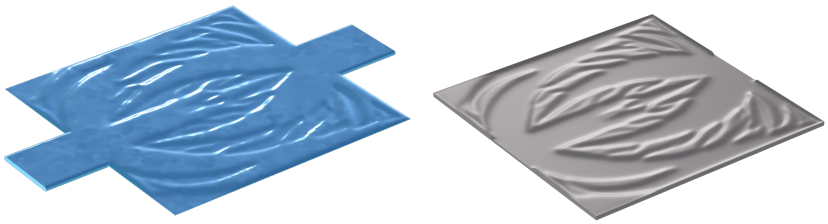

(b) Design optimised at t_{end}=30s

Fig. 15: Three-dimensional geometry of plates and channels generated based on transient optimised design.

within 1% and 2%, respectively. For the $t_{\text{end}} = 15$ s transient design, the relative error between the reduced-dimensional model and the full model is slightly larger, with a maximum error of about 6.5%. This error can be attributed to the fact that the mesh used in the full model is not sufficiently fine or that the optimisation design with $t_{\text{end}} = 15$ s has a large area of low-height areas and the accuracy of the reduced-dimensional model suffers somewhat here. Nevertheless, for this design, the error between the reduced-dimensional model and the full model was kept within 2% over the time range of $t \in [0, t_{\text{end}}]$, which is of interest to the optimisation problem.

Figure 17 shows the average temperature of the plate over time for the optimised and reference designs analysed using the full three-dimensional model. As can be seen from the graph, the transient optimised design with $t_{\text{end}} = 15$ s and the steady-state optimised design perform as expected: the average temperature of the design with $t_{\text{end}} = 15$ s is lower than that of the other designs in the short term, but when the time exceeds 15 seconds, the average temperature of this design increases rapidly and eventually becomes significantly higher than that of the other designs. The steady-state optimised design has a higher temperature in the short term than the transient optimised design, but its temperature is lowest when the operating time is long enough. However, unlike the results of the reduced-dimensional model, the temperature of the transient optimised design with $t_{\text{end}} = 30$ s is higher than that of the steady-state design at 30 s, and the lowest temperature occurs at [15, 23] s. It should be noted that the results of the reduced-dimensional model show that the temperatures of the two designs at 30 s are very close, with a difference of only 0.16 K, and are therefore highly susceptible to error. These errors may be attributed to the process of geometric reconstruction of the three-dimensional model or the coarseness of the three-dimensional mesh used for the analysis. Overall, the performance of the optimised three-dimensional model in the above verification is generally consistent with the results obtained using the reduced-dimensional model, indicating that the optimised design using the

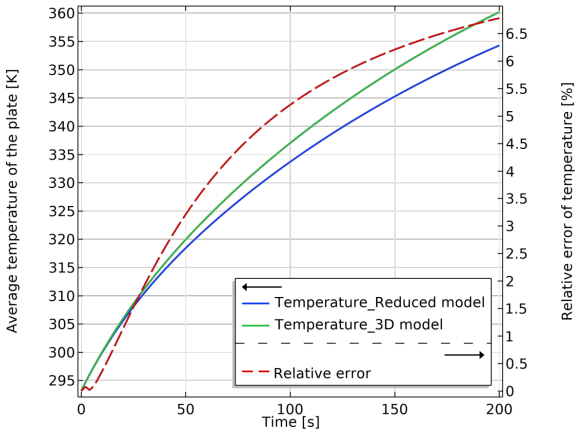

(a) Optimised design with $t_{\text{end}} = 15$s

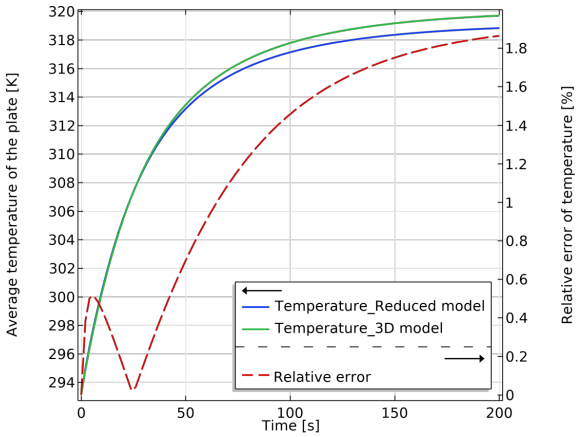

(b) Optimised design with $t_{\text{end}} = 30$s

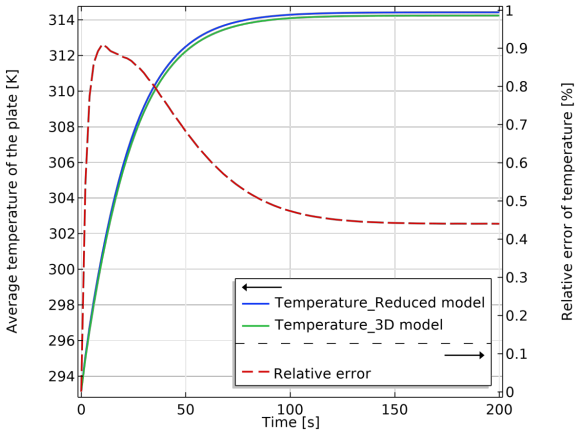

(c) Optimised design for steady state

Fig. 16: Comparison of temperatures and relative errors for [0, 200] s obtained using the reduced-dimensional model and the full model for the three optimised designs.

reduced-dimensional model are reasonably accurate.

6 Concluding remarks

This paper extends the reduced-dimensional model previously proposed by Alexandersen (2022) and Sun et al (2022), applying it to the optimisation of transient heat transfer between fluid flow and plates with a volumetric heat source. The improvement over the previous work is that the extended reduced-dimensional model introduces the temperature field of the plate with a heat source governed by the heat conduction equation and relates it to the temperature field of the fluid governed by the convection-diffusion equation through the heat flux balance equation. In addition, the paper extends the model to investigate the transient temperature response, which poses higher challenges to the accuracy and computational efficiency of the reduced-dimensional model. This paper uses a linear interpolation scheme with channel height and plate thickness as design variables and applies the extended reduced-dimensional model to the topography optimisation of plates with the objective of minimising the average temperature of the plates. The effects of different operating times on the optimised design is investigated.

By comparing the results with those of the full three-dimensional model, this paper demonstrates the accuracy and reliability of the reduced-dimensional model. Compared to the full model, the reduced-dimensional model significantly reduces the computational cost and keeps the temperature error at a single moment and the accumulated temperature error over the entire time within acceptable ranges. Based on the efficiency and reliability of the reduced-dimensional model, this paper applies the model to both steady-state and transient optimisation and demonstrates the correctness of the optimised design through crosschecks. By comparing the steady-state and transient designs, it is found that when the process of temperature variation takes up the majority of the operating time, there is a significant difference between the transient and steady-state optimised designs, and better performance can be achieved by considering the transient effect for optimisation. When the heat transfer time is longer, the transient

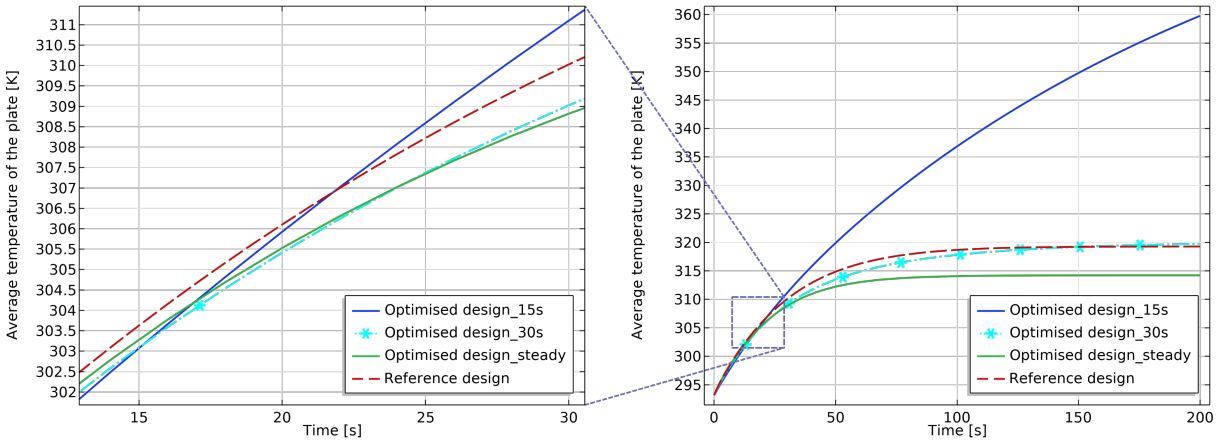

Fig. 17: Comparison of plate temperatures for different designs at [0,200] s verified using a three-dimensional model.

optimised design gradually approaches the steady-state design, and optimising the structure at the steady state can result in a satisfactory design at a relatively low computational cost. In addition, the optimised designs are verified using the full model, and the results are consistent with the optimisation process. However, due to the errors in the three-dimensional implementation process and the reduced-dimensional model itself, a certain tolerance space for errors needs to be reserved when using the reduced-dimensional model for optimisation.

Future work will focus on applying the model to solve some practical industrial heat transfer problems with more dramatic time-dependent changes in heat transfer boundary conditions and to solve some stronger nonlinear problems with temperature-dependent physical properties, such as phase change materials, which are important for thermal energy storage systems.

Statements and Declarations

Competing Interest. The authors declare that they have no conflict of interest.

CRediT authorship contribution statement. **Yupeng Sun:** Methodology, software, verification, investigation, computations, writing - original draft, writing - review & editing, visualisation. **Song Yao:** Resources, supervision, writing - review & editing, funding acquisition. **Joe Alexandersen:** Conceptualisation, methodology, investigation, resources, supervision, writing - review & editing, project administration.

Acknowledgments. The work was performed during the first author's visit to University of Southern Denmark funded by the Study Abroad Program from Central South University and the Study Abroad Scholarship from China Scholarship Council. The corresponding author was partially sponsored through the "NeGeV: Next Generation Ventilation" project funded by the Danish Energy Agency under the Energy Technology Development and Demonstration Program (EUDP project number 64017-05117). Part of the computations were performed on the UCloud interactive HPC system, which is managed by the eScience Center at the University of Southern Denmark.

Replication of results. An example COMSOL file for the transient optimisation at $t_{\text{end}} = 30$ s from Section 5.2 is available on GitHub: https://github.com/sdu-multiphysics/topography/tree/main/plateheat.

Appendix A Derivations for heat conservation equations

This section shows the derivation of the reduced-dimensional model for transient heat transfer in solids. The conservation of heat in the control volume is established as in the Eq. A1. By

substituting the profile function of temperature and integrating in the direction of thickness, the Eq. A2 can be obtained. Dividing the Eq. A2 by $\Delta x_1 \Delta x_2$, due to the size of the control volume $\Delta x_1 \to 0$ and $\Delta x_2 \to 0$, the differential equation Eq. A3 can be obtained according to the relationship between the limit and the derivative. Sorting Eq. A3 gives the final transient heat equation for solid as shown in Eq. A4.

Appendix B Mesh convergence study

In this section, the meshes used in this paper are analysed by taking the meshes used for the reduced-dimensional model and the full three-dimensional model in the verification section. For the optimisation section, the meshes they use are established in the same way as the meshes described above and are therefore not repeated.

The three-dimensional mesh used for the verification of the full three-dimensional model is shown in Fig. A1. This mesh is generated by discretizing the plane of the model using quadrilateral elements and mapping them to other surfaces. The planar mesh consists of quadrilateral elements with side length of $L/150$, with 7 layers of elements discretized in the channel height and 5 layers of elements discretized in the plate thickness. The entire mesh is consisted of 332,660 elements and the DOFs to be solved is 2,577,373, the transient solution time is 23,105 s.

The refinement of the mesh can be adjusted by adjusting the size of the planar elements and the number of layers of element in the thickness direction, the refinement of which can be expressed in terms of the number of DOFs to be solved. Figure A2 illustrates the variation of the average temperature of the plate with the DOFs. It can be seen from the figure that as the number of DOFs increases, the average temperature of the plate gradually converges and is well converged with the mesh employed in verification section, thus demonstrating the validity of the three-dimensional mesh.

The two-dimensional mesh used for the reduced-dimensional model in the verification section is shown in Fig. A3. The mesh consists of quadrilateral elements with side lengths of $L/300$. The overall mesh consists of 51,000 elements and the number of DOFs to be solved using the reduced-dimensional model is 800,874, the transient solution time is 705 s.

The refinement of the mesh is adjusted by resizing the elements, the refinement of which can be expressed in terms of the number of DOFs to be solved. Figure A4 illustrates the variation of the average temperature of the plate with the DOFs. It can be seen from the graph that the variation of the average temperature of the plate decreases as the number of DOFs increases. Although the curve shows that further refinement of the mesh is required to obtain convergence, it may need to be noted that the difference between the temperature of the coarse mesh and the fine mesh is not so large that the effectiveness of the mesh taken in this section is acceptable. Also, computational time is an important factor to take into account.

Appendix C Implementation details on volumetric heat source

In this paper, the heated plate is uniformly distributed with a volumetric heat source. The generated power is constant for the entire system and the heat source per volume varies according to the current volume of the plate, which is more consistent with the design requirements of an actual thermal system.

The volumetric heat source is calculated by the following equation:

$$Q = \frac{P}{V_{\mathrm{s}}} = \frac{P}{\int_{\omega_{\mathrm{s}}} h_{\mathrm{s}} \, dS} \tag{C5}$$

where the integration over the plate thickness in the plane $\int_{\omega_{\mathrm{s}}} h_{\mathrm{s}} \, dS$ is implemented by a non-coupled operator in COMSOL. Since the thickness of the plate is varied during the optimisation process, the volumetric heat source needs to be calculated using the above equation in each optimisation iteration. However, the integral operator will be calculated repeatedly by COMSOL's built-in analytic differentiation method for sensitivity calculation in each iteration, which greatly increases the computational cost. To address this, this work uses the nojac() operator to ignore the

$$\iiint \rho_s C_s \frac{\partial T_s}{\partial t}\, dx_3\, dx_2\, dx_1 + \iint -K_s \frac{\partial T_s}{\partial x_3}\, dx_2\, dx_1 \mid_{x_3=-\frac{h_s}{2}} - \iint -K_s \frac{\partial T_s}{\partial x_3}\, dx_2\, dx_1 \mid_{x_3=\frac{h_s}{2}}$$
$$+ \iint_{-\frac{h_s}{2}}^{\frac{h_s}{2}} -K_s \frac{\partial T_s}{\partial x_2}\, dx_3\, dx_1 \mid_{x_2=x_2} - \iint_{-\frac{h_s}{2}}^{\frac{h_s}{2}} -K_s \frac{\partial T_s}{\partial x_2}\, dx_3\, dx_1 \mid_{x_2=x_2+\Delta x_2}$$
$$+ \iint_{-\frac{h_s}{2}}^{\frac{h_s}{2}} -K_s \frac{\partial T_s}{\partial x_1}\, dx_3\, dx_2 \mid_{x_1=x_1} - \iint_{-\frac{h_s}{2}}^{\frac{h_s}{2}} -K_s \frac{\partial T_s}{\partial x_1}\, dx_3\, dx_2 \mid_{x_1=x_1+\Delta x_1}$$
$$+ \iiint Q\, dx_3\, dx_2\, dx_1 = 0 \tag{A1}$$

$$\rho_s C_s \left(\frac{\partial T_s}{\partial t} \frac{2h_s}{3} + \frac{\partial T_i}{\partial t} \frac{h_s}{3} \right) \Delta x_1 \Delta x_2 + K_s \left(T_i - T_s \right) \frac{8}{h_s} \Delta x_1 \Delta x_2$$
$$+ K_s \Delta x_1 \left(\frac{\partial T_s}{\partial x_2} \frac{2h_s}{3} + \frac{\partial T_i}{\partial x_2} \frac{h_s}{3} - \frac{\partial h_s}{\partial x_2} \frac{2}{3} \left(T_i - T_s \right) \right) \mid_{x_2}^{x_2+\Delta x_2}$$
$$+ K_s \Delta x_2 \left(\frac{\partial T_s}{\partial x_1} \frac{2h_s}{3} + \frac{\partial T_i}{\partial x_1} \frac{h_s}{3} - \frac{\partial h_s}{\partial x_1} \frac{2}{3} \left(T_i - T_s \right) \right) \mid_{x_1}^{x_1+\Delta x_1}$$
$$+ Q h_s \Delta x_1 \Delta x_2 = 0 \tag{A2}$$

$$\rho_s C_s \left(\frac{\partial T_s}{\partial t} \frac{2h_s}{3} + \frac{\partial T_i}{\partial t} \frac{h_s}{3} \right) + K_s \left(T_i - T_s \right) \frac{8}{h_s} + K_s \frac{\partial}{\partial x_2} \left(\frac{\partial T_s}{\partial x_2} \frac{2h_s}{3} + \frac{\partial T_i}{\partial x_2} \frac{h_s}{3} - \frac{\partial h_s}{\partial x_2} \frac{2}{3} \left(T_i - T_s \right) \right)$$
$$+ K_s \frac{\partial}{\partial x_1} \left(\frac{\partial T_s}{\partial x_1} \frac{2h_s}{3} + \frac{\partial T_i}{\partial x_1} \frac{h_s}{3} - \frac{\partial h_s}{\partial x_1} \frac{2}{3} \left(T_i - T_s \right) \right) + Q = 0 \tag{A3}$$

$$\rho_s C_s h_s \left(2 \frac{\partial \bar{T}_s}{\partial t} + \frac{\partial T_i}{\partial t} \right) + 24 K_s \left(\frac{\bar{T}_s - T_i}{h_s} \right) - 3 Q h_s - K_s \frac{\partial}{\partial x_i} \left(2 \frac{\partial h_s}{\partial x_i} \left(\bar{T}_s - T_i \right) + h_s \frac{\partial}{\partial x_i} \left(2 \bar{T}_s + T_i \right) \right) = 0 \tag{A4}$$

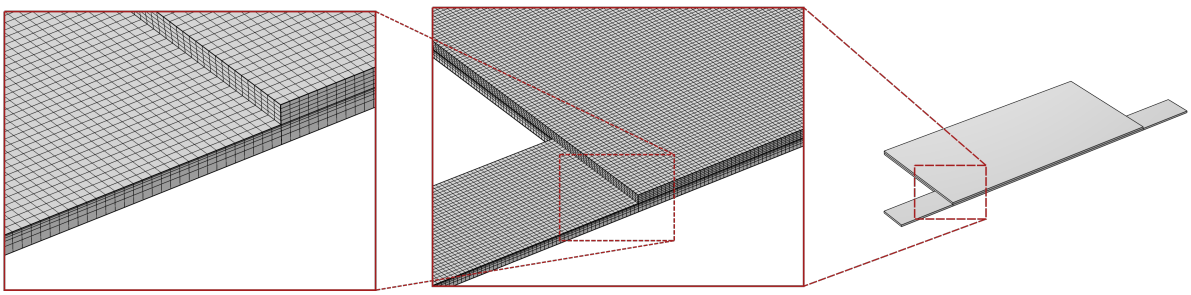

Fig. A1: Schematic diagram of the mesh used for full three-dimensional model simulations.

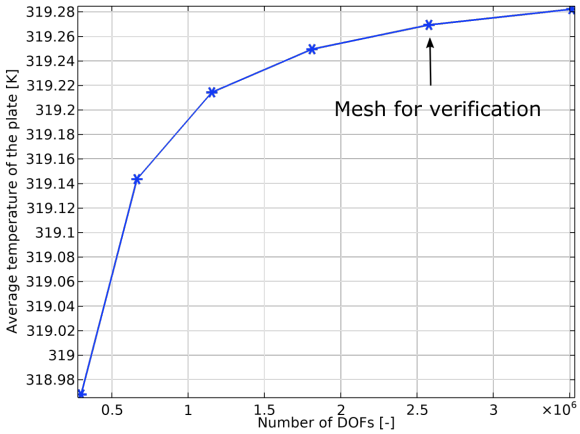

Fig. A2: The average temperature of the plate varies with the number of DOFs.

contribution of the heat source term to the sensitivity of this optimisation problem. By comparing the optimised designs obtained by considering and ignoring the heat source term in the sensitivity calculation, there is no significant difference between the two designs. However, using the nojac () operator drastically reduces the optimisation time and, therefore, this paper uses the nojac() operator for the heat source term in all the presented optimisations.

References

Abou Elmaaty TM, Kabeel AE, Mahgoub M (2017) Corrugated plate heat exchanger review. Renewable and Sustainable Energy Reviews 70:852–860. https://doi.org/10.1016/j.rser.2016.11.266

Alexandersen J (2022) Topography optimisation of fluid flow between parallel plates of spatially-varying spacing: Revisiting the origin of fluid flow topology optimisation. Structural and Multidisciplinary Optimization 65(5):152. https://doi.org/10.1007/s00158-022-03243-8

Alexandersen J, Andreasen CS (2020) A review of topology optimisation for fluid-based problems. Fluids 5(1):29. https://doi.org/10.3390/fluids5010029

Alexandersen J, Aage N, Andreasen CS, et al (2014) Topology optimisation for natural convection problems. International Journal for Numerical Methods in Fluids 76(10):699–721. https://doi.org/10.1002/fld.3954

Borrvall T, Petersson J (2003) Topology optimization of fluids in stokes flow. International Journal for Numerical Methods in Fluids 41(1):77–107. https://doi.org/10.1002/fld.426

Coffin P, Maute K (2016) A level-set method for steady-state and transient natural convection problems. Structural and Multidisciplinary Optimization 53(5):1047–1067. https://doi.org/10.1007/s00158-015-1377-y

COMSOL (2022) URL www.comsol.com

Dallaire J, Adeel Hassan HM, Bjernemose JH, et al (2022) Performance analysis of a dual-stack air-pcm heat exchanger with novel air flow configuration for cooling applications in buildings. Building and Environment 223:109450. https://doi.org/10.1016/j.buildenv.2022.109450

Dbouk T (2017) A review about the engineering design of optimal heat transfer systems using topology optimization. Applied Thermal Engineering 112:841–854. https://doi.org/10.1016/j.applthermaleng.2016.10.134

Fawaz A, Hua Y, Le Corre S, et al (2022) Topology optimization of heat exchangers: A review. Energy 252:124053. https://doi.org/10.1016/j.energy.2022.124053

Haertel JH, Engelbrecht K, Lazarov BS, et al (2018) Topology optimization of a pseudo 3d thermofluid heat sink model. International Journal of Heat and Mass Transfer 121:1073–1088. https://doi.org/10.1016/j.ijheatmasstransfer.2018.01.078

Hassan HMA, Hansen MPR, Dallaire J, et al (2023) Performance analysis of a stand-alone thermal energy storage system based on csm plates filled with phase change material. Energy and Buildings 278:112621. https://doi.org/10.1016/j.enbuild.2022.112621

Lazarov BS, Sigmund O (2011) Filters in topology optimization based on helmholtz-type differential equations. International Journal for

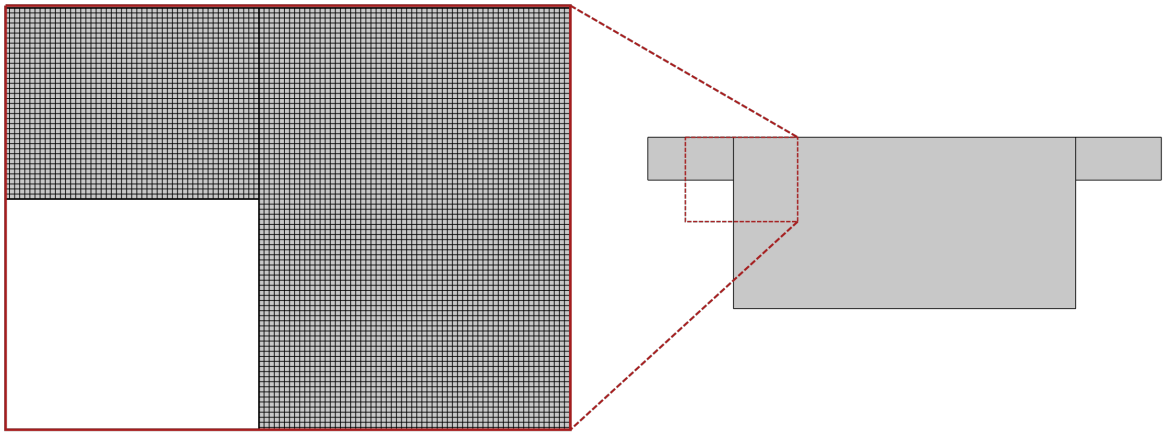

Fig. A3: Schematic diagram of the mesh used for reduced-dimensional model simulations.

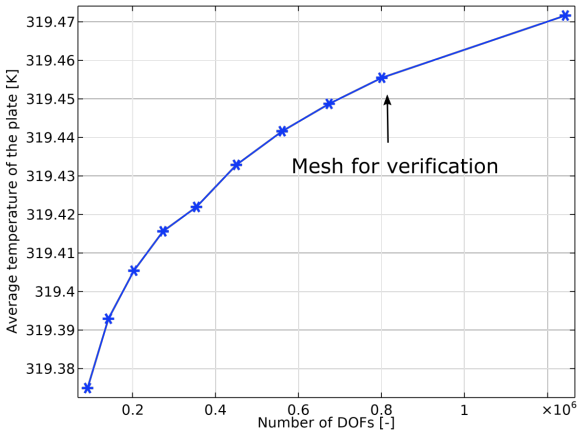

Fig. A4: The average temperature of the plate varies with the number of DOFs.

Numerical Methods in Engineering 86(6):765–781. https://doi.org/10.1002/nme.3072

Lundgaard C, Engelbrecht K, Sigmund O (2019) A density-based topology optimization methodology for thermal energy storage systems. Structural and Multidisciplinary Optimization 60(6):2189–2204. https://doi.org/10.1007/s00158-019-02375-8

Pizzolato A, Sharma A, Maute K, et al (2017) Design of effective fins for fast pcm melting and solidification in shell-and-tube latent heat thermal energy storage through topology optimization. Applied Energy 208:210–227. https://doi.org/10.1016/j.apenergy.2017.10.050

Pizzolato A, Sharma A, Ge R, et al (2020) Maximization of performance in multi-tube latent heat storage – optimization of fins topology, effect of materials selection and flow arrangements. Energy 203:114797. https://doi.org/10.1016/j.energy.2019.02.155

Sun Y, Yao S, Alexandersen J (2022) Topography optimisation using a reduced-dimensional model for convective heat transfer between plates with varying channel height and constant temperature. Under review in Structural and Multidisciplinary Optimization (4232895). https://doi.org/10.2139/ssrn.4232895

Sun Y, Hassan HMA, Alexandersen J (2023) Application of a reduced-dimensional model for fluid flow between stacks of parallel plates with complex surface topography. Fluids 8(6). https://doi.org/10.3390/fluids8060174

Tanabe Y, Yaji K, Ushijima K (2023) Topology optimization using the lattice boltzmann method for unsteady natural convection problems. Structural and Multidisciplinary Optimization 66(5):103. https://doi.org/10.1007/s00158-023-03522-y

Tong Z, Yang Q, Tong S, et al (2022) Two-stage thermal-hydraulic optimization for pillow plate heat exchanger with recirculation zone parameterization. Applied Thermal Engineering 215:119033. https://doi.org/10.1016/j.applthermaleng.2022.119033

Veje CT, Jradi M, Lund I, et al (2019) Negev: next generation energy efficient ventilation system using phase change materials. Energy Informatics 2(1):2. https://doi.org/10.1186/s42162-019-0067-1

Yaji K, Ogino M, Chen C, et al (2018) Large-scale topology optimization incorporating local-in-time adjoint-based method for unsteady thermal-fluid problem. Structural and Multidisciplinary Optimization 58(2):817–822. https://doi.org/10.1007/s00158-018-1922-6

Yan S, Wang F, Hong J, et al (2019) Topology optimization of microchannel heat sinks using a two-layer model. International Journal of Heat and Mass Transfer 143:118462. https://doi.org/10.1016/j.ijheatmasstransfer.2019.118462

Yoon GH (2010) Topological design of heat dissipating structure with forced convective heat transfer. Journal of Mechanical Science and Technology 24(6):1225–1233. https://doi.org/10.1007/s12206-010-0328-1

Zeng S, Lee PS (2019) Topology optimization of liquid-cooled microchannel heat sinks: An experimental and numerical study. International Journal of Heat and Mass Transfer 142:118401. https://doi.org/10.1016/j.ijheatmasstransfer.2019.07.051

Zeng S, Kanargi B, Lee PS (2018) Experimental and numerical investigation of a mini channel forced air heat sink designed by topology optimization. International Journal of Heat and Mass Transfer 121:663–679. https://doi.org/10.1016/j.ijheatmasstransfer.2018.01.039

Zeng T, Wang H, Yang M, et al (2020) Topology optimization of heat sinks for instantaneous chip cooling using a transient pseudo-3d thermofluid model. International Journal of Heat and Mass Transfer 154:119681. https://doi.org/10.1016/j.ijheatmasstransfer.2020.119681

Zhao J, Zhang M, Zhu Y, et al (2021a) Topology optimization of planar cooling channels using a three-layer thermofluid model in fully developed laminar flow problems. Structural and Multidisciplinary Optimization 63(6):2789–2809. https://doi.org/10.1007/s00158-021-02842-1

Zhao J, Zhang M, Zhu Y, et al (2021b) Topology optimization of turbulent forced convective heat sinks using a multi-layer thermofluid model. Structural and Multidisciplinary Optimization 64(6):3835–3859. https://doi.org/10.1007/s00158-021-03064-1

Zhu K, Chang Z, Li M, et al (2023) Design, optimization and experimental testing of 2 k cryogenic plate-fin heat exchanger. Applied Thermal Engineering 223:119973. https://doi.org/10.1016/j.applthermaleng.2023.119973